DRAFT VERSION JANUARY 10, 2025
Typeset using LaTeX **twocolumn** style in AASTeX631

# Spectropolarimetric Inversion in Four Dimensions with Deep Learning (SPIn4D): II. A Physics-Informed Machine Learning Method for Vector Magnetic Field Disambiguation and Geometric Height Prediction

KAI E. YANG (杨凯) [1], XUDONG SUN (孙旭东) [1], JIAYI LIU (刘嘉奕) [2], PETER SADOWSKI [3], S. CURT DODDS [2], LUCAS A. TARR [4], MATTHIAS REMPEL [5], SARAH A. JAEGGLI [4], THOMAS A. SCHAD [4], IAN CUNNYNGHAM [2], YANNIK GLASER [3], AND LINNEA WOLNIEWICZ [3]

[1] *Institute for Astronomy, University of Hawai'i at Mānoa, Pukalani, HI 96768, USA*
[2] *Institute for Astronomy, University of Hawai'i at Mānoa, Honolulu, HI 96822, USA*
[3] *Department of Information and Computer Sciences, University of Hawai'i at Mānoa, Honolulu, HI 96822, USA*
[4] *National Solar Observatory, Pukalani, HI 96768, USA*
[5] *High Altitude Observatory, NSF National Center for Atmospheric Research, Boulder, CO 80307, USA*

## ABSTRACT

The spectropolarimetric inversion of vector magnetic fields faces a well-known problem of 180-degree ambiguity in the azimuth angle. Traditionally, this challenge is tackled by minimizing a target function, such as the divergence of the magnetic field within a single layer. On the other hand, the geometric height of a single optical depth layer is usually not a flat plane, known as the Wilson depression in the sunspot. The technique of solving this height is limited. We introduce a novel approach using the Physics-Informed Machine Learning technique to solve the divergence-free equation of the magnetic field across multiple optical depth layers, while simultaneously estimating the geometric heights of these layers. Our approach has been tested on magnetohydrodynamic simulations of both quiet Sun, plage region, and sunspot, effectively recovering the horizontal field orientation on pixels with strong magnetic fields. By combining the disambiguated vector magnetic field with the estimated geometric heights, our method can reconstruct the three-dimensional vector electric currents in the solar photosphere.

*Keywords:* Solar atmosphere (1477) — Solar photosphere (1518) — Solar magnetic fields (1503) — Computational methods (1965) — Convolutional neural networks (1938)

## 1. INTRODUCTION

Solar magnetic field measurements are one of the major and challenging tasks in the solar atmosphere diagnostic. The magnetic field dominates many phenomena and is the energy source for many activities in the solar atmosphere, like solar flares, coronal mass ejections, and coronal heating. The measurements are usually done in the lower solar atmosphere, like the photosphere and chromosphere, which could provide a bottom boundary for analyzing those activities. The measuring technique of the vector magnetic field in the solar photosphere is usually based on the inversion of the spectropolarimetric data (del Toro Iniesta & Ruiz Cobo 2016; Bellot Rubio & Orozco Suárez 2019). However, these inversions intrinsically inherent a 180-degree ambiguity of the azimuth angle (Harvey 1969), i.e., two possible choices differ by 180 degrees. This introduces uncertainty to the vector magnetic field for further analysis, like the extrapolation of the field into the corona, flare forecast, data-driving simulation, electric current, flow computations, energy, and helicity flux (Wiegelmann & Sakurai 2021; Bobra & Couvidat 2015; Kusano et al. 2020; Jiang et al. 2016; Kazachenko et al. 2014; Liu & Schuck 2012).

Various methods have been proposed for the disambiguity task in the past decades. For example, the Acute Angle Method and its improved version compare the observed field to an extrapolated field, like the potential field or the linear force-free field, to determine the orientation of the transverse field (Wang 1997; Wang et al. 2001; Moon et al. 2003). An interactive utility AZAM software for the HAO/NSO Advanced Stokes Polarimeter (Elmore et al. 1992) minimizes the angle between neighbor pixels. The Non-potential Magnetic Field Calculation (NPFC, Georgoulis 2005), requires the computation of a proxy electric current density, whose first version degenerates with the potential field acute an-

Corresponding author: Kai E. Yang
yangkai@hawaii.edu

gle method when applied to disk center observations and the refined version NPFC2 was improved by implementing with the parity-free absolute vertical current density (Semel & Skumanich 1998). The Minimum Energy method (ME0, Metcalf 1994) tries to minimize a function that contains the residual divergence of the magnetic field and the electric current by simulating an annealing process, and it is widely used in many data pipelines, like the Helioseismic and Magnetic Imager (HMI, Scherrer et al. 2012; Hoeksema et al. 2014; Liu et al. 2017) and Hinode Solar Optical Telescope/Spectro-Polarimeter (SOT/SP, Tsuneta et al. 2008) products. An improved version with temporal evolution was proposed as well (Barnes et al. 2018). More techniques and their performance and comparison can be found in the technique reviews (Metcalf et al. 2006; Leka et al. 2009b, 2012, and reference therein). Many of the above-mentioned methods assume the magnetic field lies on a flattened plane, and some of them even contain derivatives of the magnetic field, which is valid when the computational plane is flattened, or the vertical fluctuation is small compared to the transverse spatial resolution in practice.

Meanwhile, straightforward methods for this problem have been discussed. For example, the ambiguity of the inverted transverse field can be solved by multi-view measurements with at least 0.1 radians away from the Sun-Earth line (Judge 2019), which has been realized (Valori et al. 2022, 2023) by coordinate observation from *Solar Orbiter* (*SolO*, Müller et al. 2020) and *Solar Dynamic Observatory* (*SDO*, Pesnell et al. 2012). However, such observations are highly limited, and their spatial resolution is not high enough to study the small-scale structure, like the details in the quiet Sun granules and photosphere bright points. Also, a spectroscopic method based on resonance line has been discussed (Landi Degl'Innocenti & Bommier 1993), like Sr I 4607 Å. However, as pointed by Judge (2019) such particular radiation transitions might not happen in the photosphere, where many magnetic field deducing is focused, and observing the polarization signal from this line is difficult (Malherbe et al. 2007; Bianda et al. 2018; Dhara et al. 2019; Zeuner et al. 2018, 2020, 2022, 2024).

With the operation of advanced huge ground-based telescopes, like the National Science Foundation's *Daniel K. Inouye Solar Telescope* (DKIST, Rimmele et al. 2020), high spatially resolved observations have been provided (down to $0.03''$). With the help of the large aperture (4 m) of DKIST and excellent seeing condition at Haleakalā, the high polarized signals can be achieved ($\approx 5 \times 10^{-4}$, Rimmele et al. 2020; de Wijn et al. 2022; Jaeggli et al. 2022; Harrington et al. 2023). More accurate and detailed physics information in solar atmosphere can be obtained by applying the sophisticated inversion techniques to DKIST observations. For example, Stokes Inversion based on Response functions (SIR, Ruiz Cobo & del Toro Iniesta 1992), Departure coefficient aided SIR (DeSIRe, Ruiz Cobo et al. 2022), Stokes-Profiles-INversion-O-Routines (SPINOR, Frutiger et al. 2000; van Noort 2012), HAnle and ZEeman Light (HAZEL, Asensio Ramos et al. 2008), Non-LTE Inversion COde using the Lorien Engine (NICOLE, Socas-Navarro et al. 2015), SNAPI (Milić & van Noort 2018), STockholm Inversion Code (STiC, de la Cruz Rodríguez et al. 2019), and FIRTEZ (Pastor Yabar et al. 2019) can provide the magnetic field information on multiple optical depth layers, from where the spectral lines provide strong response to the magnetic parameters.

It is worth noting that the inverted magnetic field by the above-mentioned advanced techniques lies on the optical depth layers rather than the geometric layers. The solar surface with a certain optical depth is depressed in the sunspots relative to the quiet Sun, which is known as Wilson depression (Wilson & Maskelyne 1774). Since the strong magnetic field in the sunspot reduces the gas pressure and suppresses convection, leading to a relatively low temperature and low opacity. This depression also happened with high spatial resolved quiet Sun and the plage regions with strong magnetic fields that are illustrated by state-of-the-art solar simulations (see Figures 4 and 12 in Yang et al. 2024). Several methods to quantify this depression have been proposed based on the force balance between pressure gradient, gravity, and Lorentz force (Martinez Pillet & Vazquez 1993; Mathew et al. 2004), which has been improved by implementing the divergence-free condition of the magnetic field (Puschmann et al. 2010). Furthermore, it has been shown that high accurate magnetic field equipped with divergence-free condition is enough to decode the Wilson depression (Löptien et al. 2018, 2020). On the other hand, with the help of magnetohydrostatic (MHS), some complex methods that combine the Stokes inversion with the force balance can handle this problem as well, like the FIRTEZ code and its application of the Hinode observations (Pastor Yabar et al. 2019; Borrero et al. 2019, 2021; Borrero & Pastor Yabar 2023; Borrero et al. 2024). A more completed method that combines magnetohydrodynamics (MHD) and Stokes inversion is applied to Sunrise/IMaX observation (Riethmüller et al. 2017) that can provide a full set of atmospheric parameters. Recently, the Polarimetric and Helioseismic Imager (PHI, Solanki et al. 2020) onboard *SolO* provide a direct measurement of the large-scale geometric height by doing stereoscopy technique (Romero Avila et al. 2024). However, this method is based on limited spacecraft missions. It is important to note that most of the methods mentioned above require a disambiguated vector magnetic field before decoding the geometric height. Considering the difficulties of the aforementioned disambiguity techniques, it indicates that the ambiguity and the Wilson depression are closely tangled.

Recent advancements in machine learning (ML) techniques have demonstrated their utility in solar physics (Asensio Ramos et al. 2023). A notable example is the Stokes Inversion based on Convolutional Neural Networks (SICON, Asensio Ramos & Díaz Baso 2019) and its application (Esteban Pozuelo et al. 2024), which employs convolutional neural networks (CNNs) trained on Max-Planck University-of-Chicago Radiative MHD (MURaM, Vögler et al. 2005; Rempel et al. 2009) sunspot simulations (Rempel 2012) and synthesized Stokes profiles to directly infer physical and geometric parameters, although it does not address the 180-degree ambiguity. Despite its effectiveness, this supervised ML approach requires extensive computational resources due to the large volume of simulations. Alternative methods that leverage the existing extensive results from conventional inversion techniques in the solar physics community have also been proposed as well (Higgins et al. 2021, 2022). Taking a step forward, the Spectropolarimetric Inversion in Four Dimensions with Deep Learning (SPIn4D) project[1] leverages solar atmosphere data of quiet Sun and plage regions from MURaM simulations, encompassing a total of 110 TB of data, and is developing an advanced ML model for analyzing DKIST observed Stokes profiles, an overview of SPIn4D can be found in Yang et al. (2024).

Supervised machine ML models benefit from data generated by advanced radiative MHD simulations. However, due to the lack of in-situ measurements of the solar photosphere, these models may face the issues of out-of-distribution (Hendrycks & Gimpel 2017).

> *Models trained by MURaM simulation will predict like a MURaM.*[2]

Moreover, interpreting the trained neural networks presents significant challenges (Zeiler & Fergus 2014), raising concerns about their reliability when applied to real observations. Alternatively, when encoding the physics law into the ML technique, a lot of new techniques to solve the physics problem have been proposed (E & Yu 2018; Sirignano & Spiliopoulos 2018; Lu et al. 2021; Hennigh et al. 2021), which is known as physics-informed machine learning (PIML, Karniadakis et al. 2021; Kashinath et al. 2021; Hao et al. 2022; Wu et al. 2024, and references therein). PIML can work with relatively small datasets while ensuring that predictions obey the physical laws, i.e., solve the partial differential equations (PDE). One of them is the physics-informed neural network (PINN, Raissi 2018; Raissi et al. 2019). This approach facilitates inversion tasks and achieves accuracy comparable to traditional computational fluid dynamics methods (Mao et al. 2020). Such methods have been introduced into solar physics problems as well, which are flexible for handling data from different instruments with different spatial resolutions (Jarolim et al. 2023, 2024a,b). Furthermore, such architectures can seamlessly combine multiple tasks simultaneously using surrogate models and custom loss functions. However, the PINN architectures are usually used for a surrogate model with respect to the spatial and temporal coordinates and relatively less learning from the observational data patterns.

Resolving the resulting three dimensional (3D) data ambiguity resembles a data translation task, a common approach in ML. The UNet model (Ronneberger et al. 2015), widely used for image segmentation and translation and integral to generative artificial intelligence models (Isola et al. 2017; Ho et al. 2020), is well-suited for such tasks. Since the magnetic field parameters derived from Stokes profiles with advanced inversion techniques span 3D, two spatial dimensions from the field-of-view (FOV), and one from optical depth. Utilizing the 3D UNet model, UNet3D (Çiçek et al. 2016; Wolny et al. 2020), combined with physics-informed constraints, particularly the divergence-free condition, crucial for both disambiguation (Metcalf 1994) and Wilson depression (Löptien et al. 2018), might provide an alternative way for addressing the two tangled challenges, i.e., 180-degree ambiguity and geometric height estimation, without relying on a specific numerical simulation model.

In this paper, as the second paper of the SPIn4D project, we propose a novel method, `Haleakala Disambiguation Decoder` (HDD), based on the PIML technique that can solve the 180-degree ambiguity of the transverse field and the associated geometric height from multilayer inversion at the same time. It is accessible on GitHub[3]. The paper is organized as follows. Section 2 presents the design of the network and training process. Section 3 presents the test of this technique and a comparison with the conventional method. Sections 4 and 5 present the discussion and summary.

## 2. METHOD

### 2.1. *Model and Encoding the Physics*

Our network architecture integrates two UNet3D models based on the `ResidualUNet3D` module (Lee et al. 2017) from the `pytorch-3dunet` package (Wolny et al. 2020). Each model consists of 4 layers with feature maps of 64, 128, 256, and 512 channels, respectively. Hereafter, "UNet3D" refers to the `ResidualUNet3D` module. The first model, UNet3D$_B$, is tasked with disambiguating the magnetic field, while the second, UNet3D$_Z$, predicts geometric heights. The models process five-dimensional input data. The initial two dimensions correspond to the batch and channel sizes of the

[1] https://ifauh.github.io/SPIN4D/

[2] A comment from SHINE Workshop 2022.

[3] https://github.com/Kai-E-Yang/HDD

data. Specific details regarding the batch size will be provided in Section 3. We define the channel size as six to encompass the components of ambiguated magnetic fields and an initial estimate of geometric height. One channel refers to the vertical magnetic field, and four channels refer to the transverse field components modulated into $[0, \pi]$ and $[-\pi/2, \pi/2]$. The final three dimensions of the input represent spatial coordinates $x$, $y$, and $z$. The outputs from UNet3D$_B$ and UNet3D$_Z$ consist of three channels for the magnetic field and one channel for the geometric height, respectively. Thus, each batch of training data yields predictions for both the magnetic field ($B_{x,ijk}$, $B_{y,ijk}$, $B_{z,ijk}$) and geometric height $Z_{ijk}$, where $i$, $j$, and $k$ indicate the pixel indexes along $\hat{x}$, $\hat{y}$, and $\hat{z}$ directions.

A difference between the predicted magnetic field and the input ambiguated magnetic field is included in the custom loss function.

$$loss_{B_z} = \text{mean}(\frac{(B_{z,pred} - B_{z,input})^4}{B_{z,input}^2 + 10^{-8}}), \tag{1}$$

$$loss_{B_t} = \text{mean}(\frac{(B_{x,pred}^2 + B_{y,pred}^2 - B_{x,input}^2 - B_{y,input}^2)^2}{B_{x,input}^2 + B_{y,pred}^2 + 10^{-8}}), \tag{2}$$

where we only measure that for the vertical and transverse magnitude without ambiguity. The small numbers $10^{-8}$ in the denominator are added for numerical stability.

Since the 180-degree problem of azimuth angle, the correct predicted transverse magnetic field should be parallel or anti-parallel to the input transverse magnetic field. This property will be protected by minimizing the square of the cross-product between the two transverse fields,

$$loss_{parallel} = \text{mean}(\frac{(B_{x,pred}B_{y,input} - B_{y,pred}B_{x,input})^2}{|B_{input}|^2 + 10^{-8}}). \tag{3}$$

Apart from the regulation by the input magnetic in magnitude and parallization. We also integrate the divergence-free condition, $\nabla \cdot \mathbf{B} = 0$, into our custom loss function. This approach ensures that the training process specifically targets minimizing the net magnetic flux residuals across each grid cell within the predicted dataset, described in the following details.

The predicted dataset has the same dimensions as the input, so each pixel contains a predicted vector magnetic field and a geometric height. Since the data is observed from a specific FOV, the transverse coordinates are predetermined: $X_{ijk} = i\Delta x + X_{\text{min}}$ and $Y_{ijk} = j\Delta x + Y_{\text{min}}$, where $\Delta x$ and $\Delta y$ refer to the spatial size in $\hat{x}$ and $\hat{y}$ directions, respectively. Therefore, each mesh cell contains eight nodes: $\vec{r}_{i,j,k}$, $\vec{r}_{i+1,j,k}$, $\vec{r}_{i,j+1,k}$, $\vec{r}_{i+1,j+1,k}$, $\vec{r}_{i,j,k+1}$, $\vec{r}_{i+1,j,k+1}$, $\vec{r}_{i,j+1,k+1}$, and $\vec{r}_{i+1,j+1,k+1}$, where $\vec{r}$ indicates the pixel coordinate vector, as illustrated in Figure 1. We calculate the net magnetic flux across all surfaces of each cell, and the mean value of these net fluxes over the entire dataset serves as a measure of the divergence-free quality. This mean flux is added to the custom loss function, and by minimizing it, we achieve the desired disambiguated magnetic field.

The surfaces of each cell shown in Figure 1(a) can be classified into three groups: lateral surfaces (transparent yellow), top surfaces (red), and bottom surfaces (blue). The lateral surfaces are denoted as

$$\begin{aligned}
S_{l,1} =&(\vec{r}_{i,j,k}, \vec{r}_{i+1,j,k}, \vec{r}_{i+1,j,k+1}, \vec{r}_{i,j,k+1}),\\
S_{l,2} =&(\vec{r}_{i+1,j,k}, \vec{r}_{i+1,j+1,k}, \vec{r}_{i+1,j+1,k+1}, \vec{r}_{i+1,j,k+1}),\\
S_{l,3} =&(\vec{r}_{i+1,j+1,k}, \vec{r}_{i,j+1,k}, \vec{r}_{i,j+1,k+1}, \vec{r}_{i+1,j+1,k+1}),\\
S_{l,4} =&(\vec{r}_{i,j+1,k}, \vec{r}_{i,j,k}, \vec{r}_{i,j,k+1}, \vec{r}_{i,j+1,k+1}).
\end{aligned}$$

The top surfaces as

$$\begin{aligned}
S_{top,1} =&(\vec{r}_{i,j,k+1}, \vec{r}_{i+1,j,k+1}, \vec{r}_{i+1,j+1,k+1}),\\
S_{top,2} =&(\vec{r}_{i,j,k+1}, \vec{r}_{i+1,j+1,k+1}, \vec{r}_{i,j+1,k+1}).
\end{aligned}$$

The bottom surfaces as

$$\begin{aligned}
S_{bottom,1} =&(\vec{r}_{i,j,k}, \vec{r}_{i+1,j,k}, \vec{r}_{i+1,j+1,k}),\\
S_{bottom,2} =&(\vec{r}_{i,j,k}, \vec{r}_{i+1,j+1,k}, \vec{r}_{i,j+1,k}).
\end{aligned}$$

The area of these four lateral surfaces, $A(\text{surface})$, can be easily computed,

$$\begin{aligned}
A(S_{l,1}) = 0.5\Delta x(&Z_{i,j,k+1} - Z_{i,j,k}\\
&+Z_{i+1,j,k+1} - Z_{i+1,j,k}),\\
A(S_{l,2}) = 0.5\Delta y(&Z_{i+1,j,k+1} - Z_{i+1,j,k}\\
&+Z_{i+1,j+1,k+1} - Z_{i+1,j+1,k}),\\
A(S_{l,3}) = 0.5\Delta x(&Z_{i+1,j+1,k+1} - Z_{i+1,j+1,k}\\
&+Z_{i,j+1,k+1} - Z_{i,j+1,k}),\\
A(S_{l,4}) = 0.5\Delta y(&Z_{i,j+1,k+1} - Z_{i,j+1,k}\\
&+Z_{i,j,k+1} - Z_{i,j,k}).
\end{aligned}$$

The magnetic fluxes across these four lateral surfaces are,

$$\begin{aligned}
Flux(S_{l,1}) = 0.25A(S_{l,1}) \times (&B_{y,i,j,k} + B_{y,i+1,j,k}\\
&+B_{y,i+1,j,k+1} + B_{y,i,j,k+1})\\
Flux(S_{l,2}) = 0.25A(S_{l,2}) \times (&B_{x,i+1,j,k} + B_{x,i+1,j+1,k}\\
&+B_{x,i+1,j+1,k+1} + B_{x,i+1,j,k+1})\\
Flux(S_{l,3}) = 0.25A(S_{l,3}) \times (&B_{y,i+1,j+1,k} + B_{y,i,j+1,k}\\
&+B_{y,i,j+1,k+1} + B_{y,i+1,j+1,k+1})\\
Flux(S_{l,4}) = 0.25A(S_{l,4}) \times (&B_{x,i,j+1,k} + B_{x,i,j,k}\\
&+B_{x,i,j,k+1} + B_{x,i,j+1,k+1}).
\end{aligned}$$

Calculating the fluxes across the top surfaces is somewhat complex because the two triangles forming these surfaces are

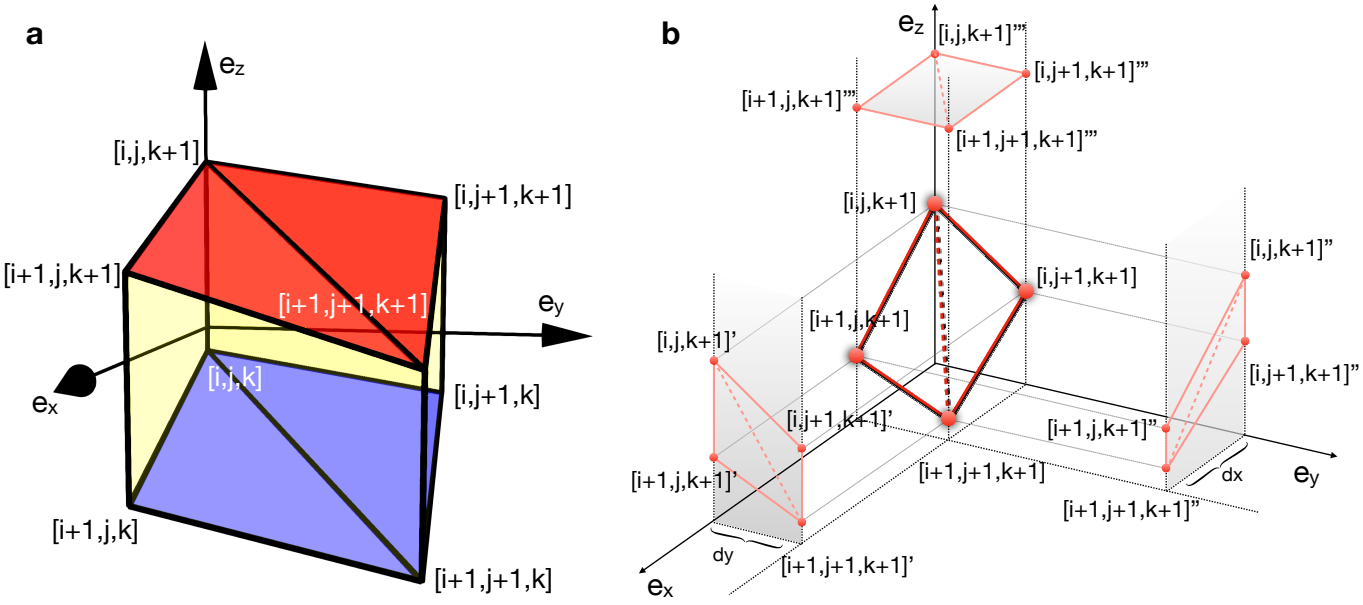


**Figure 1.** Panel (a) and (b) show the cell structure and the projected surface for the top surface, respectively.

not necessarily coplanar, the same complexity applies to the bottom surfaces. We choose to project the two triangular simplices of the top and bottom surfaces onto planes perpendicular to $\hat{x}$, $\hat{y}$, and $\hat{z}$ rather than projecting the vector magnetic field onto the normal direction of the irregular triangle surface. This allows the fluxes across them to be computed as the sum of the flux from each component. An example of the top surface is presented in Figure 1(b). The projected areas on the $\hat{x}$-perpendicular plane are

$$\begin{aligned} A_x(S_{top,1}) =& 0.5\Delta y(Z'_{i+1,j,k+1} - Z'_{i,j,k+1}), \\ A_x(S_{top,2}) =& 0.5\Delta y(Z'_{i,j+1,k+1} - Z'_{i+1,j+1,k+1}). \end{aligned}$$

Those on the $\hat{y}$-perpendicular plane are

$$\begin{aligned} A_y(S_{top,1}) =& 0.5\Delta x(Z''_{i+1,j,k+1} - Z''_{i+1,j+1,k+1}), \\ A_y(S_{top,2}) =& 0.5\Delta x(Z''_{i,j,k+1} - Z''_{i,j+1,k+1}), \end{aligned}$$

where the superscripts $'$ and $''$ indicate variables projected onto the $\hat{x}$- and $\hat{y}$-perpendicular planes, respectively. The projected areas on the $\hat{z}$-perpendicular plane are

$$\begin{aligned} A_z(S_{top,1}) =& 0.5\Delta x\Delta y, \\ A_z(S_{top,2}) =& 0.5\Delta x\Delta y. \end{aligned}$$

Therefore, the fluxes are

$$\begin{aligned} Flux(S_{top,1}) =& A_x(S_{top,1}) \times (B_{x,i,j,k+1} + \\ & B_{x,i+1,j,k+1} + B_{x,i+1,j+1,k+1})/3 \\ & + A_y(S_{top,1}) \times (B_{y,i,j,k+1} + \\ & B_{y,i+1,j,k+1} + B_{y,i+1,j+1,k+1})/3 \\ & + A_z(S_{top,1}) \times (B_{z,i,j,k+1} + \\ & B_{z,i+1,j,k+1} + B_{z,i+1,j+1,k+1})/3, \\ Flux(S_{top,2}) =& A_x(S_{top,2}) \times (B_{x,i,j,k+1} + \\ & B_{x,i+1,j+1,k+1} + B_{x,i,j+1,k+1})/3 \\ & + A_y(S_{top,2}) \times (B_{y,i,j,k+1} + \\ & B_{y,i+1,j+1,k+1} + B_{y,i,j+1,k+1})/3 \\ & + A_z(S_{top,2}) \times (B_{z,i,j,k+1} + \\ & B_{z,i+1,j+1,k+1} + B_{z,i,j+1,k+1})/3. \end{aligned}$$

The fluxes on the bottom surfaces can be computed similarly, but their surface normal orientations are reversed compared to those of the top surfaces. Finally, we compute the total flux of each cell as

$$\begin{aligned} Flux_n =& [Flux(S_{l,1}) + Flux(S_{l,2}) + Flux(S_{l,3}) \\ & + Flux(S_{l,4}) + Flux(S_{top,1}) + Flux(S_{top,2}) \\ & + Flux(S_{bottom,1}) + Flux(S_{bottom,2})]. \end{aligned}$$

The final loss flux is

$$loss_{div} = \text{mean}\left(\frac{Flux_n^4}{\text{avg}(B_x)^2 + \text{avg}(B_y) + \text{avg}(B_z)^2 + 10^{-8}}\right), \quad (4)$$

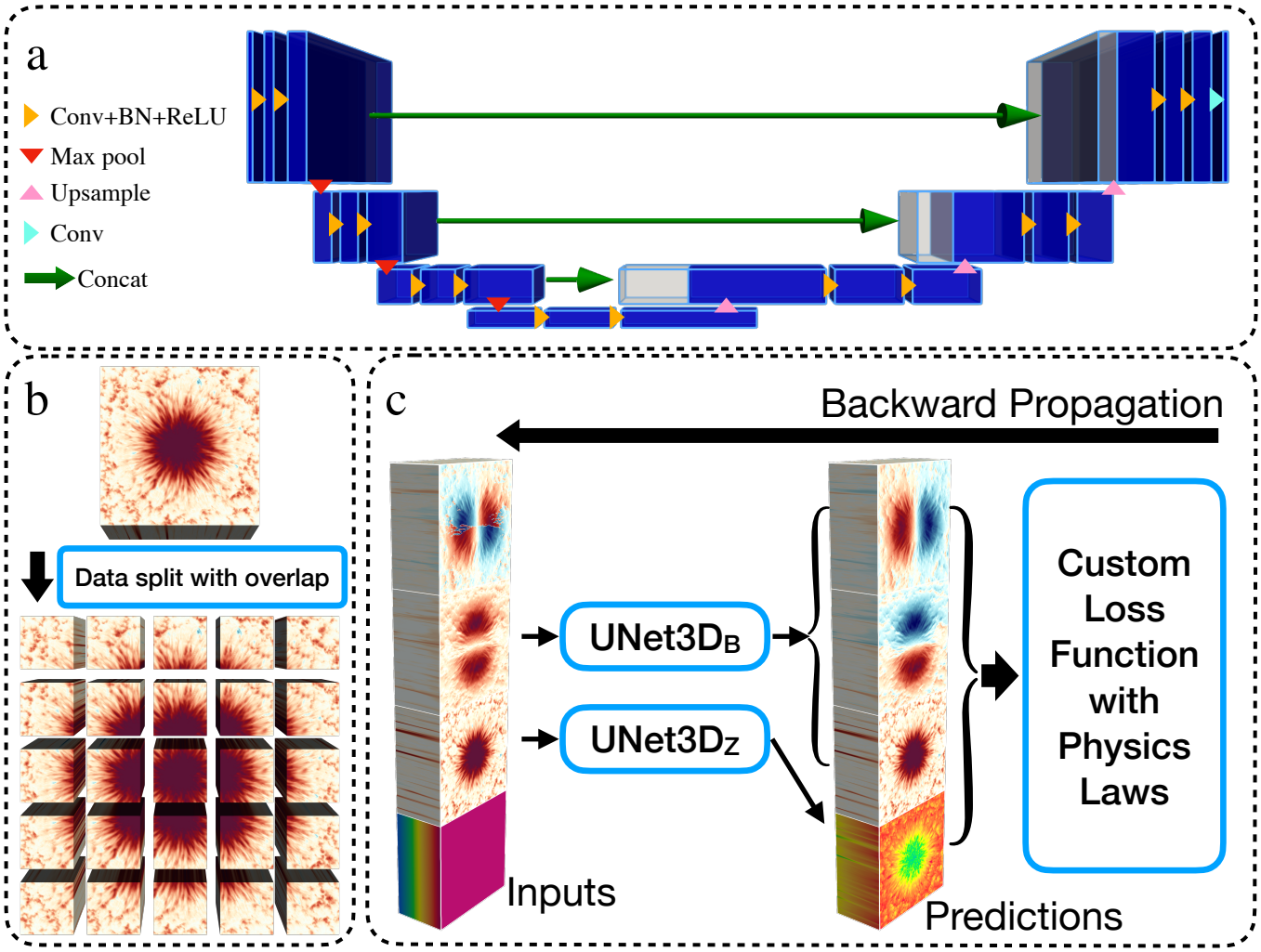


**Figure 2.** Panel (a) presents the UNet3D structure reproduced based on Figure 2 in Çiçek et al. (2016). Panel (b) shows an example of the 3D data split with overlap that prepares the input data for training. Panel (c) presents the flowchart for training the model. The inputs are the 3D ambiguity magnetic vector field and an initial guess of geometric height. The UNet3D$_B$ predicts the vector magnetic field, and UNet3D$_Z$ provides the geometric height. They are collected to compute the custom loss function with physics law encoded as shown in Equation 6.

where $\mathrm{avg}(\cdot)$ represents the average function across the eight nodes in one cell. The small number $10^{-8}$ added in the denominator enhances numerical stability. To enhance training stability, we introduce an additional function, denoted as $loss_{div,0}$, which approximates the net residual flux across each cell. This function is similar to Equation 4, but applies a fixed thickness based on the average MURaM simulation value of 7.2 km. We tested this parameter with various values and found the results to be insensitive to changes. The contribution from this term is minimized after a certain training epoch by reducing its weight to a negligible value, as detailed in Section 2.2.

Moreover, in order to make the predicted 3D geometric smooth, we added an additional 3D median filter in the predicted geometric height in the custom loss function,

$$loss_{smooth} = \mathrm{mean}([Z - \mathrm{median}(Z)]^2), \tag{5}$$

where we use a kernel size of 5 pixels.

Since the direct predicted geometric height should keep a monotonous increase in $\hat{z}$ direction. In this way, we manually add a loss term,

$$loss_{mon} = \max\{0, -(\delta Z - \delta Z_{min})\},$$

where $\delta Z_{i,j,k} = Z_{i,j,k+1} - Z_{i,j,k}$ the thickness of the optical depth layers, $\delta Z_{min} = 1.1$ km is a predetermined minimum thickness value from the MURaM quiet Sun simulation, with the thickness of $\delta\tau = 0.1$. By preventing this term from being positive, the monotonousness of $Z$ can be kept. We will always set a very large value for its weight.

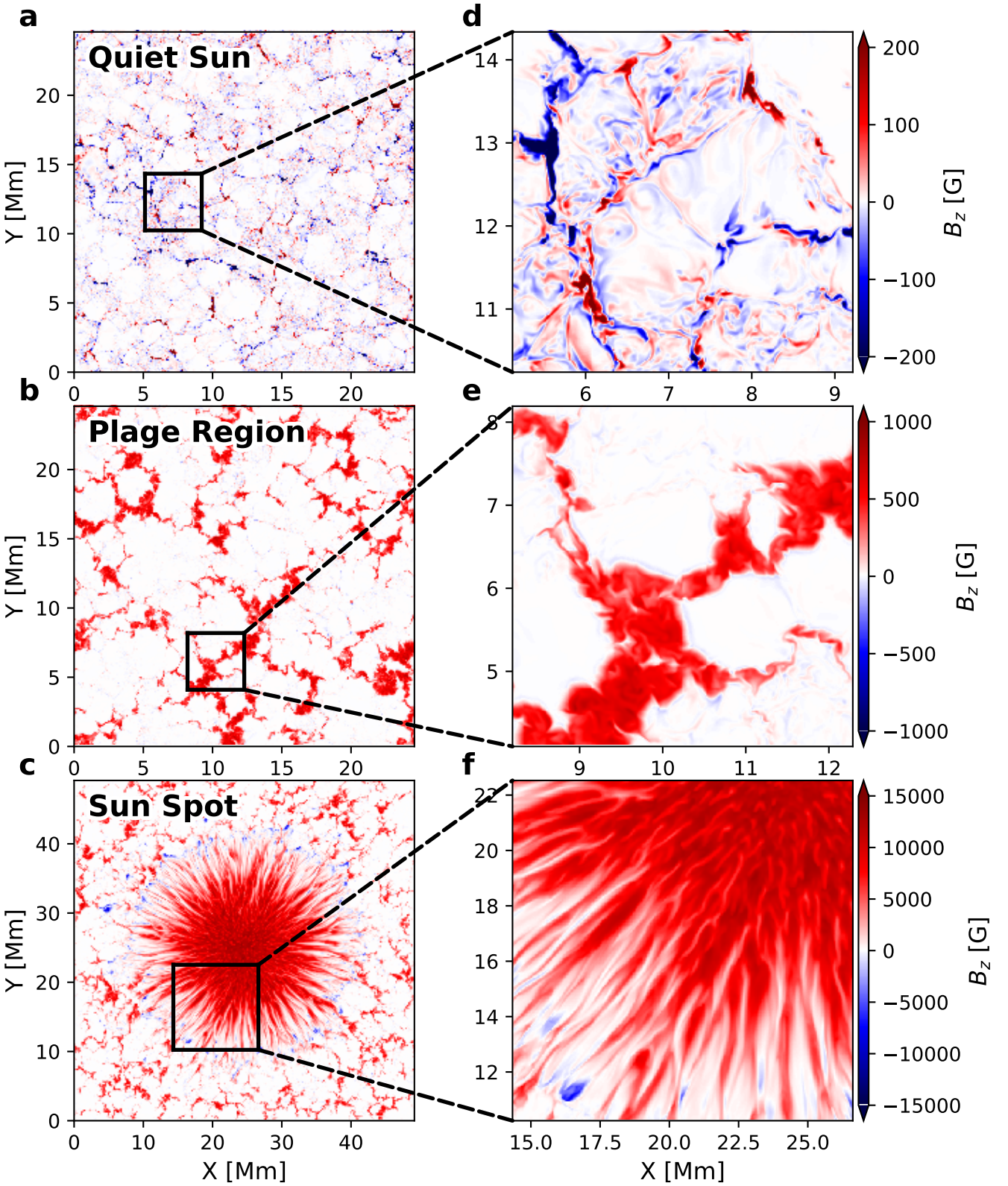


**Figure 3.** Panels (a)–(c) present the vertical components of the magnetic field, $B_z$, lay on $\log_{10}\tau = -1$ layers for the quiet Sun, plage region, and sunspot cases that used to test. The panels (d)–(f) indicate the corresponding subset test in Section 3.

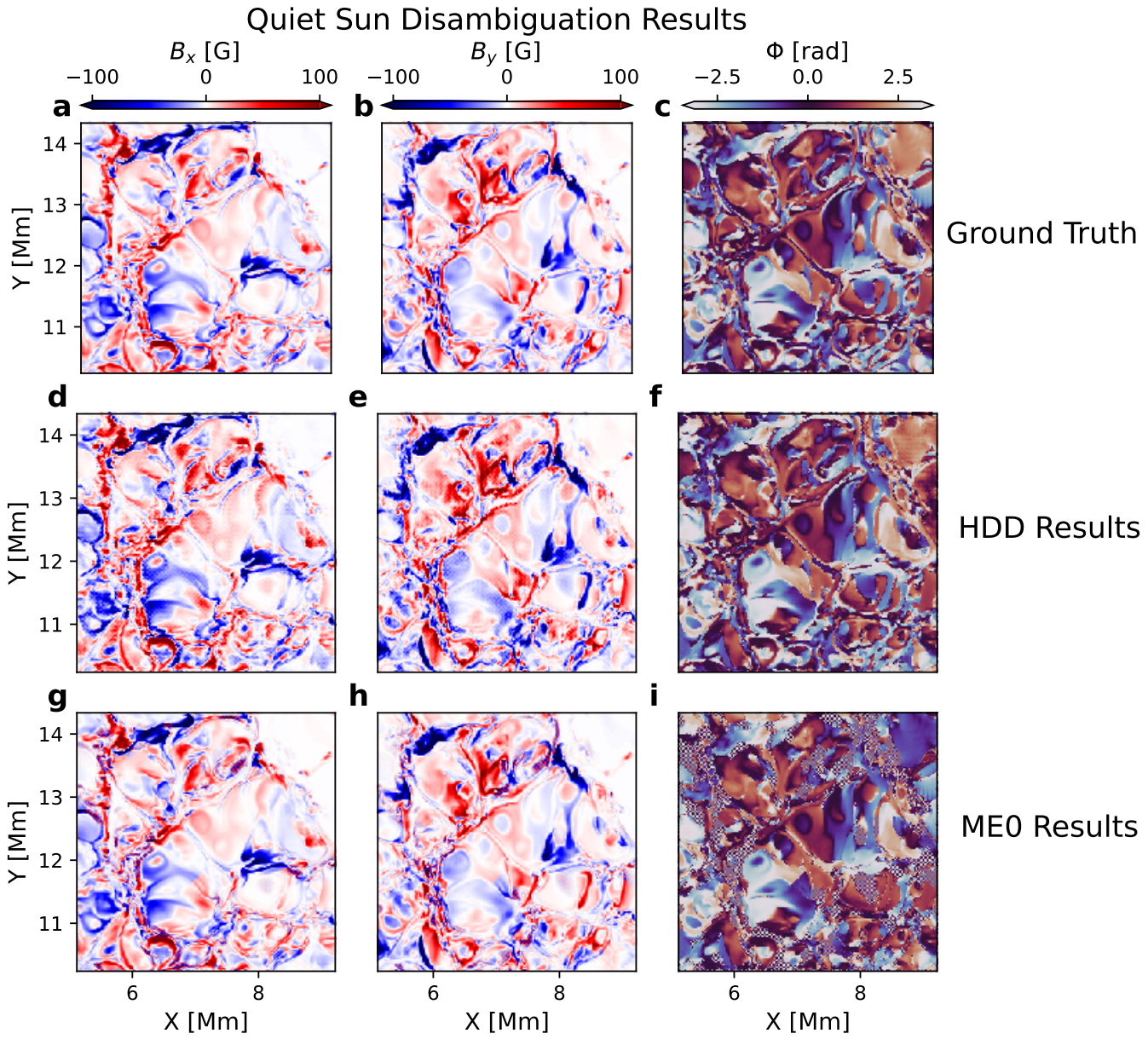


**Figure 4.** Disambiguation results for the quiet Sun test on $\log_{10}\tau = -1$ layers, the same region as Figure 3(d). Columns, from left to right, show disambiguated $B_x$, $B_y$, and azimuth angle $\Phi$. Rows, from top to bottom, present the ground truth, HDD results, and ME0 results, respectively.

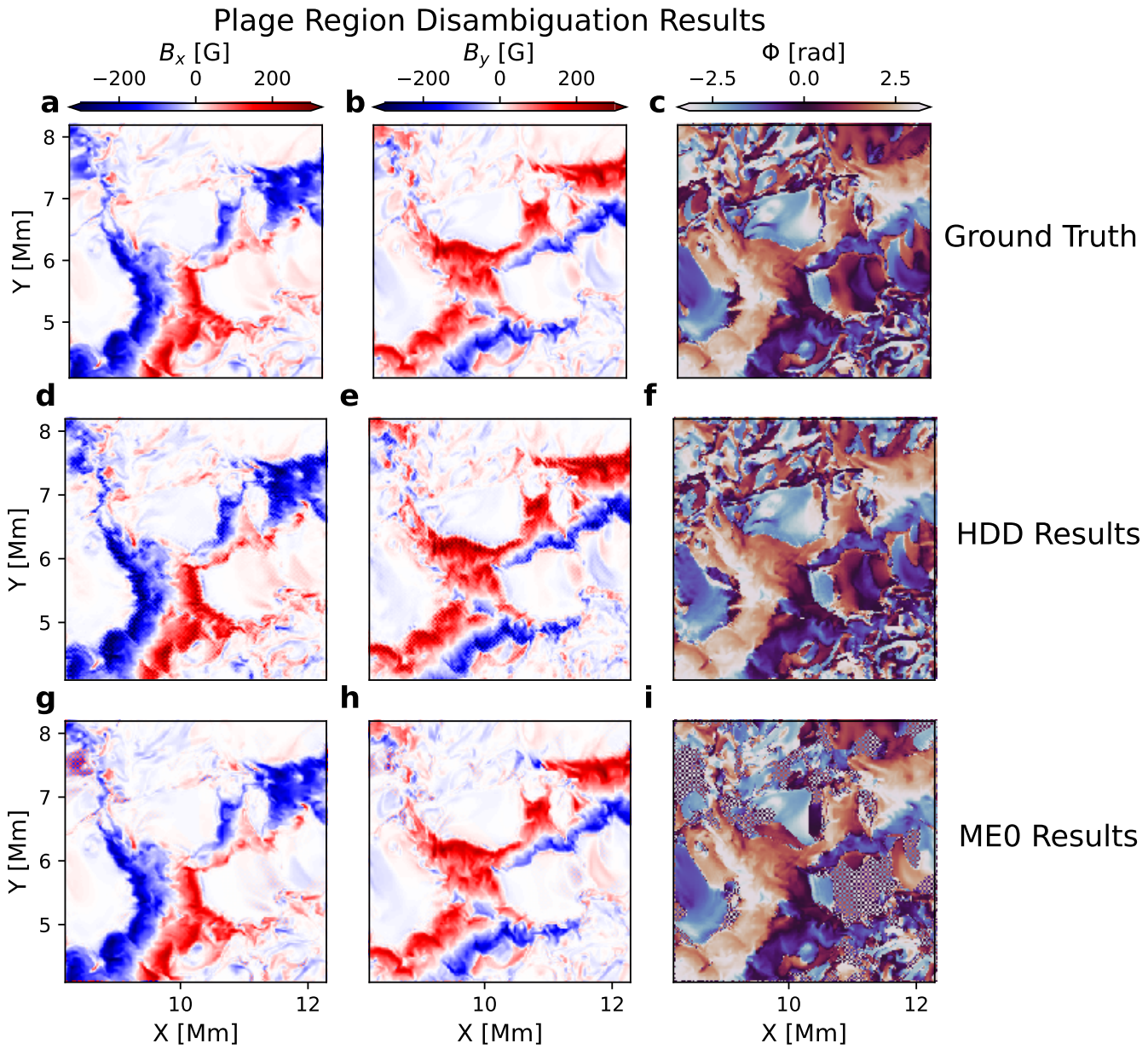


**Figure 5.** The same as Figure 4 but for the plage region dataset that shown in Figure 3(e).

The final custom loss function is,

$$\begin{aligned} loss = & w_{B_z} loss_{B_z} + w_{B_t} loss_{B_t} \\ & + w_{parallel} loss_{parallel} + w_{div} loss_{div} \\ & + w_{div,0} loss_{div,0} + w_{smooth} loss_{smooth} \\ & + w_{mon} loss_{mon}. \end{aligned} \tag{6}$$

The weight value for each loss term is discussed in Section 3.

### 2.2. *Training Strategy*

To train the model with magnetic field data from Stokes inversion, we partition the dataset into smaller, overlapping patches of size $96 \times 96 \times 32$ pixels. An overlap of 16 pixels is introduced along both the $x$- and $y$-dimensions between neighboring patches to maintain spatial continuity and capture features that extend across patch boundaries. This overlapping strategy ensures that important spatial information is preserved, enabling the model to learn both local and global patterns effectively. This overlapping split strategy is widely used when training a UNet model (Ronneberger et al. 2015; Çiçek et al. 2016; Isensee et al. 2021). The overlapped

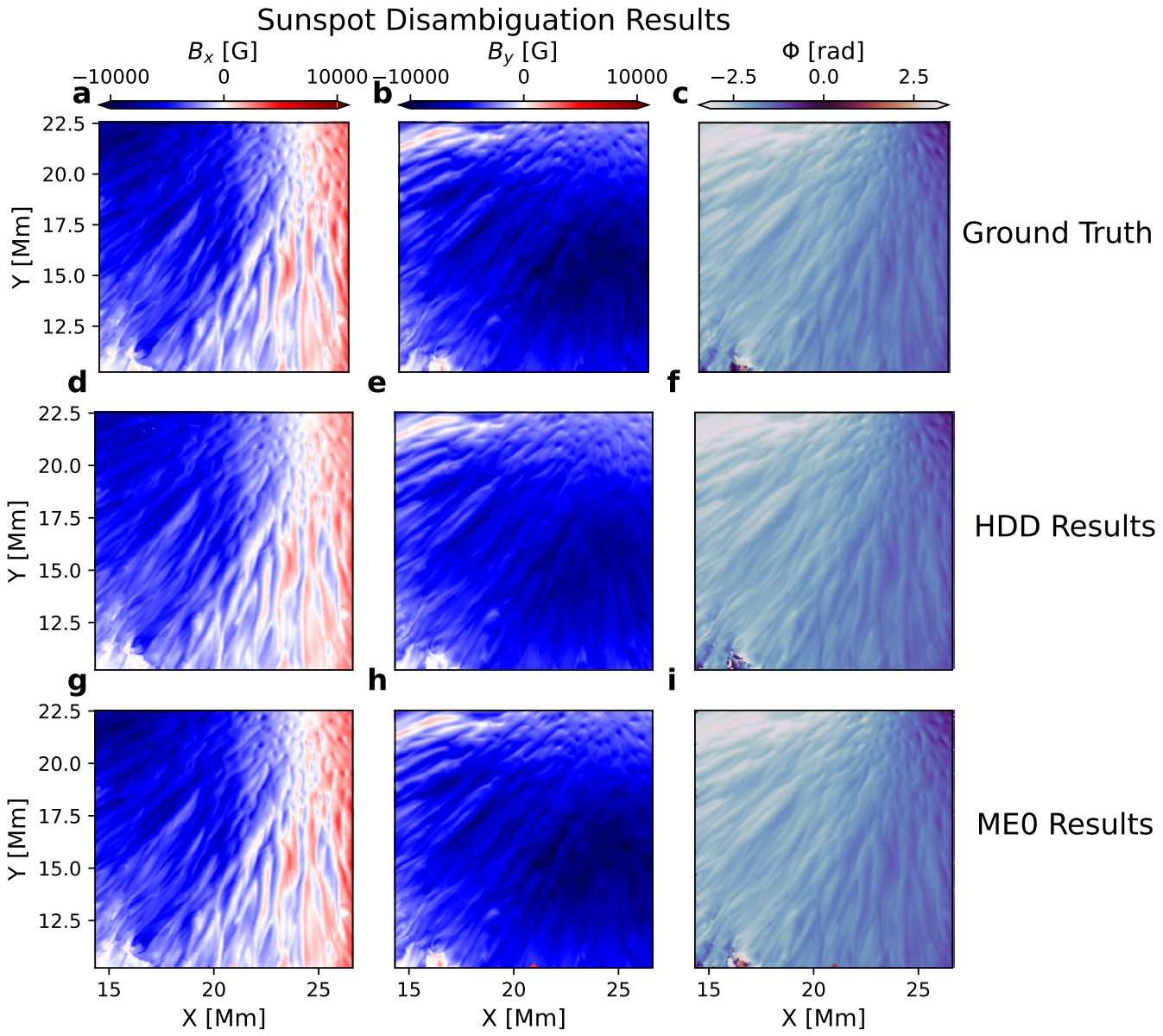


**Figure 6.** The same as Figure 4 but for the sunspot dataset that shown in Figure 3(f).

patches are then aggregated into batches for network training, which enhances the model's ability to capture variations in magnetic fields and generalize better to unseen data. This process is illustrated in Figure 2(b).

Two neural network models, Unet3D$_B$ and Unet3D$_Z$, are trained simultaneously to address both the ambiguity and geometric height. During each training epoch, these models generate predictions by processing the input data through their respective network architectures. Multiple loss components, as outlined in Equation 6, are computed for each model to capture various training objectives, including data fitting accuracy, regularization terms, and adherence to physical constraints intrinsic to the domain. The weight value for each loss term is summarized in Table 1.

Backpropagation (Rumelhart et al. 1986) is employed to compute the gradients of the total loss with respect to the model parameters. Before the optimizer updates the parameters, an adaptive gradient clipping technique is applied. This method scales and clips the gradients to prevent issues like exploding gradients, ensuring numerical stability and more reliable convergence during training. It maintains an exponential moving average (EMA) of gradient values, which allows for adaptive clipping thresholds based on the historical behavior of the gradients. First, a norm-based clipping scales

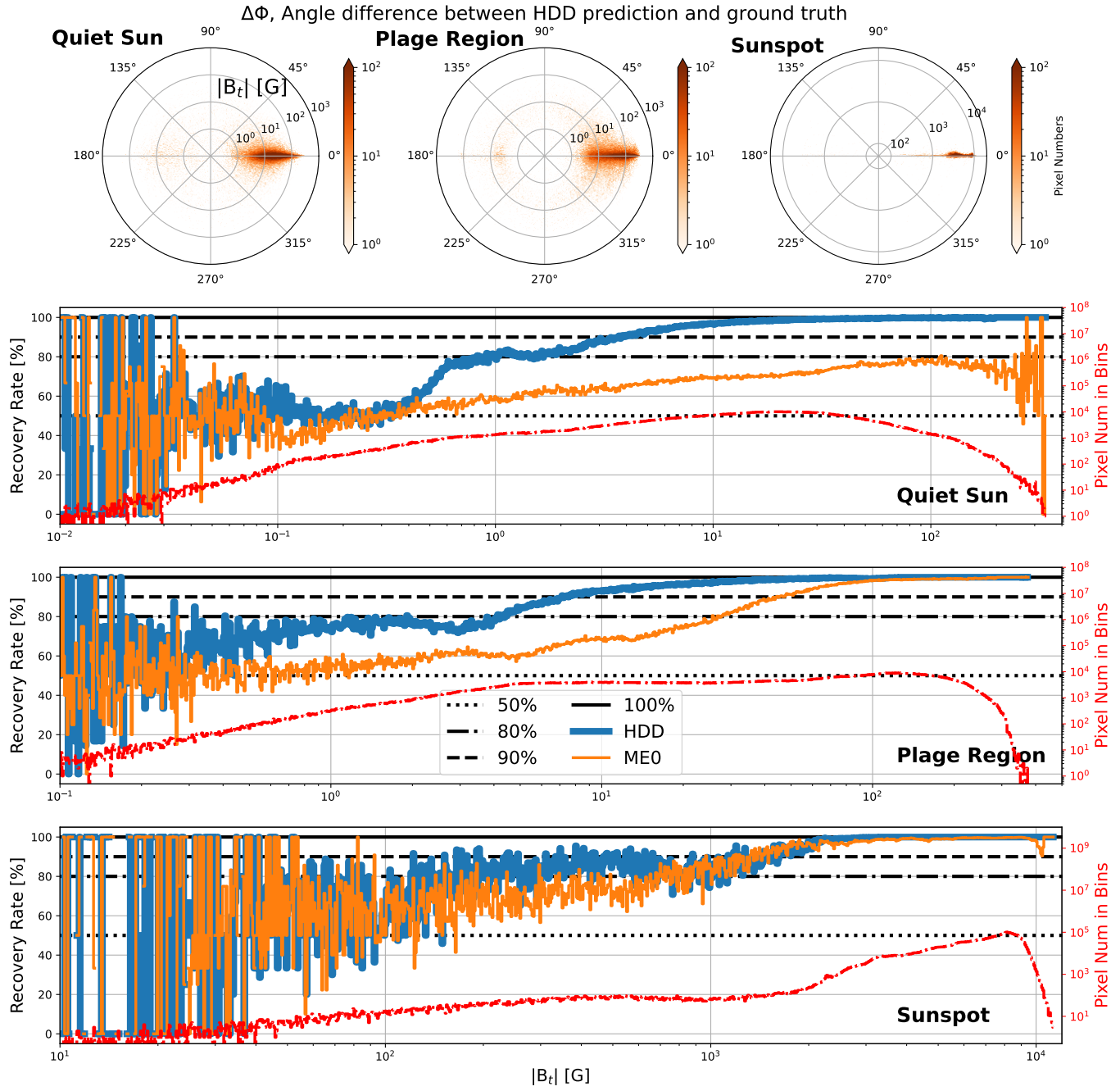


**Figure 7.** The top row displays the distribution of azimuth angle differences between the HDD prediction and ground truth in polar plots, with radius indicating transverse magnetic field strength. From left to right, the plots represent the quiet sun, plage region, and sunspot, respectively. The subsequent rows show the azimuth angle recovery rate for both HDD and ME0 results as a function of transverse field strength. The red dash-dot line represents the pixel counts within the horizontal bins corresponding to the values of $|B_t|$. The black solid, dashed, dash-dot, and dotted lines indicate the 100%, 90%, 80%, and 50% correct recovery rate, respectively.

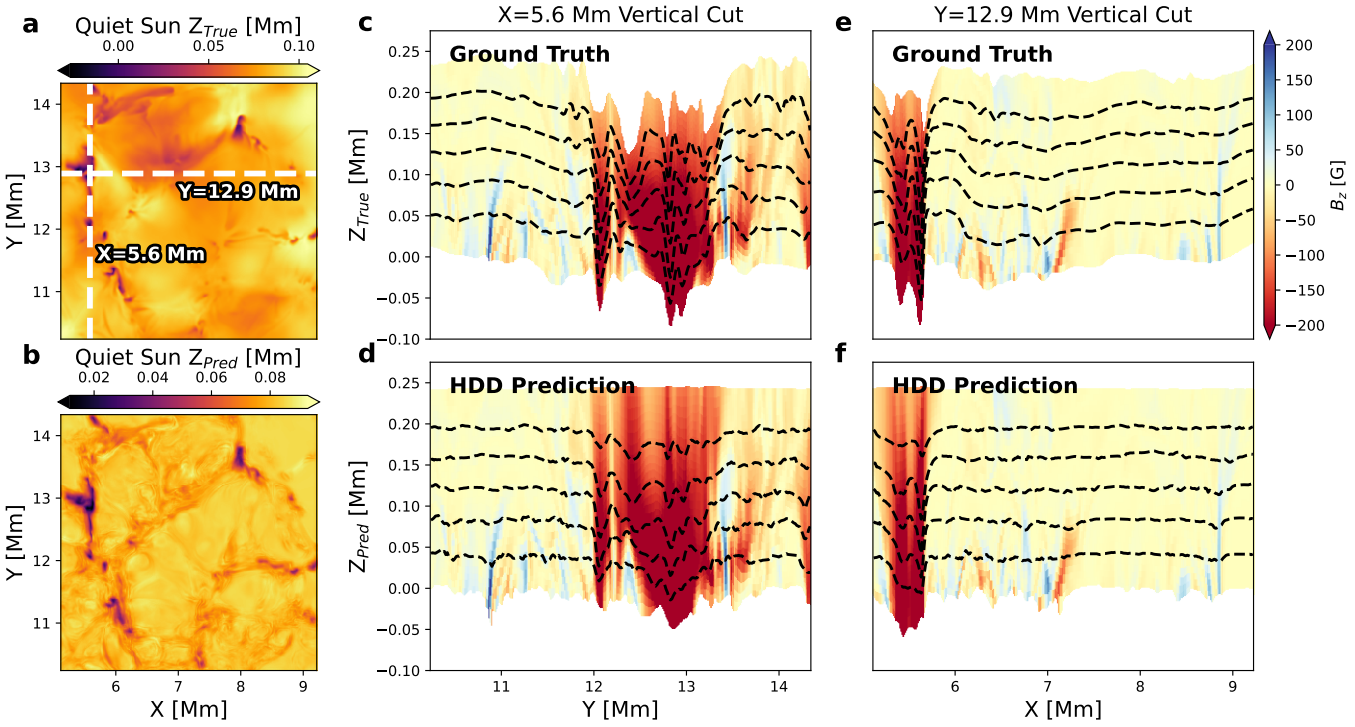


**Figure 8.** Geometric results for the QS region. Panels (a) and (b) present the true and predicted height values on the $\log_{10}\tau = -1$ layer. Panels (c)–(f) show vertical height cuts across the optical depth range $\log_{10}\tau = 0$ to $-3.1$, with color representing the $B_z$ distribution. Dashed black lines indicate $\log_{10}\tau$ values of $-0.5$, $-1$, $-1.5$, $-2.0$, and $-2.5$. Panels (c) and (e) display ground truth at vertical cuts $X = 5.6$ Mm and $Y = 12.9$ Mm, respectively, while (d) and (f) show the corresponding predictions.

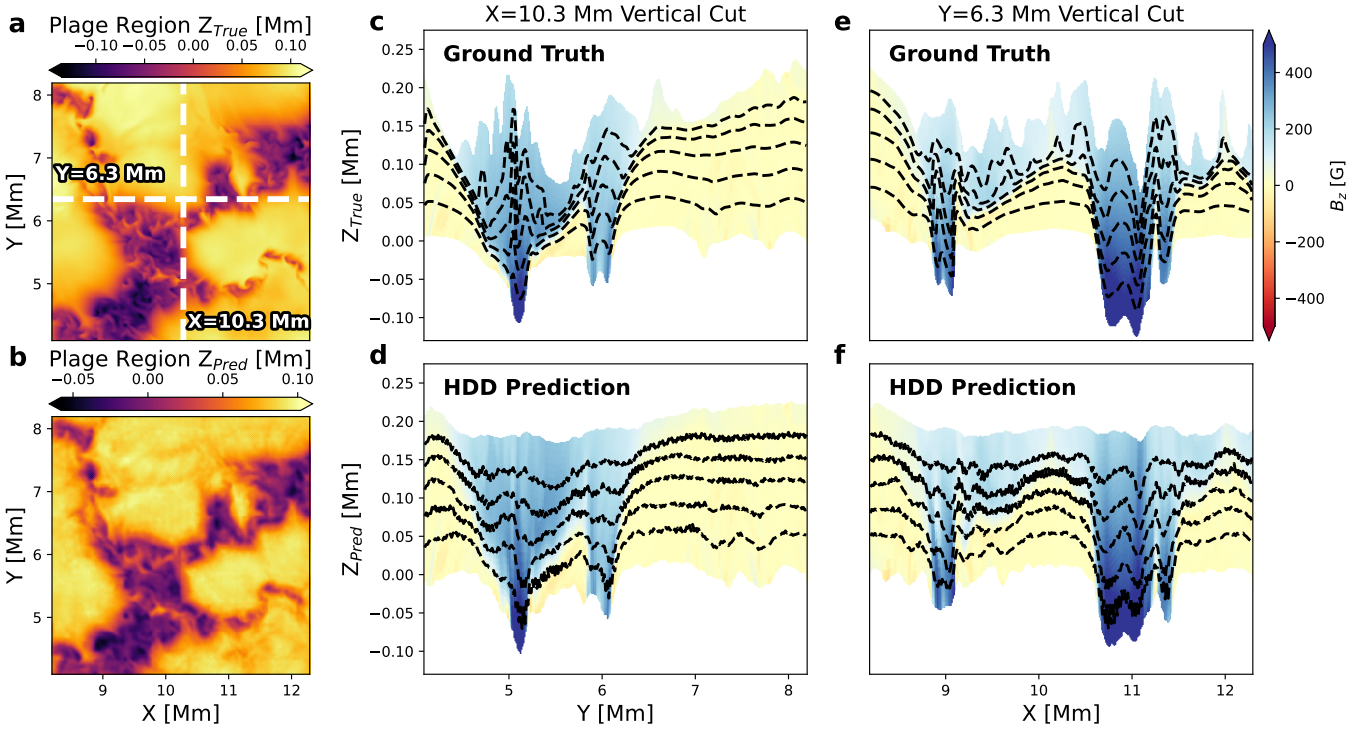


**Figure 9.** The same as Figure 8 but for the plage region results.

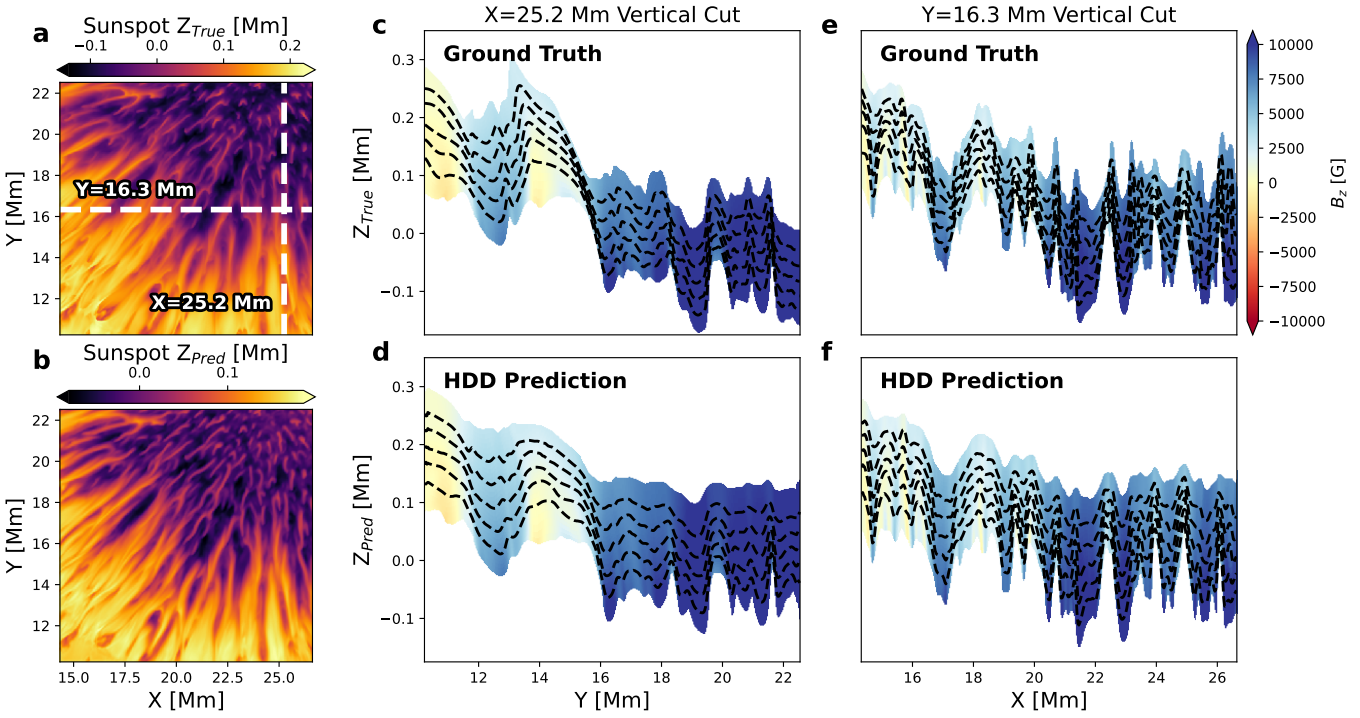


**Figure 10.** The same as Figure 8 but for the sunspot results.

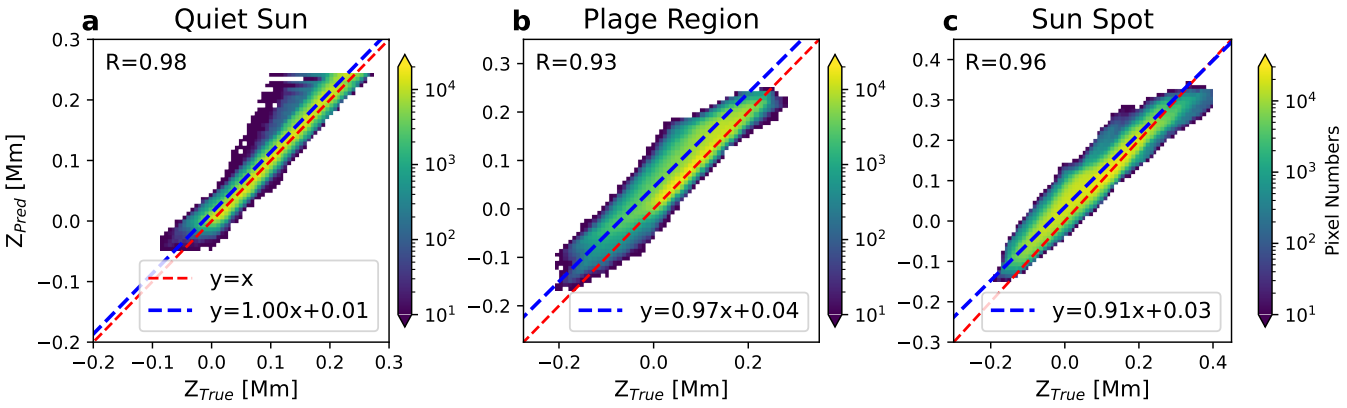


**Figure 11.** 2D histogram of predicted vs. true heights, $Z_{Pred}$ and $Z_{True}$. Panels (a)–(c) show results for quiet Sun, plage region, and sunspot, respectively. Red and blue dashed lines denote the identity and best linear fit (using $|B_t|$ as the weighting factor.), and $R$ marks the Pearson correlation coefficients for each case.

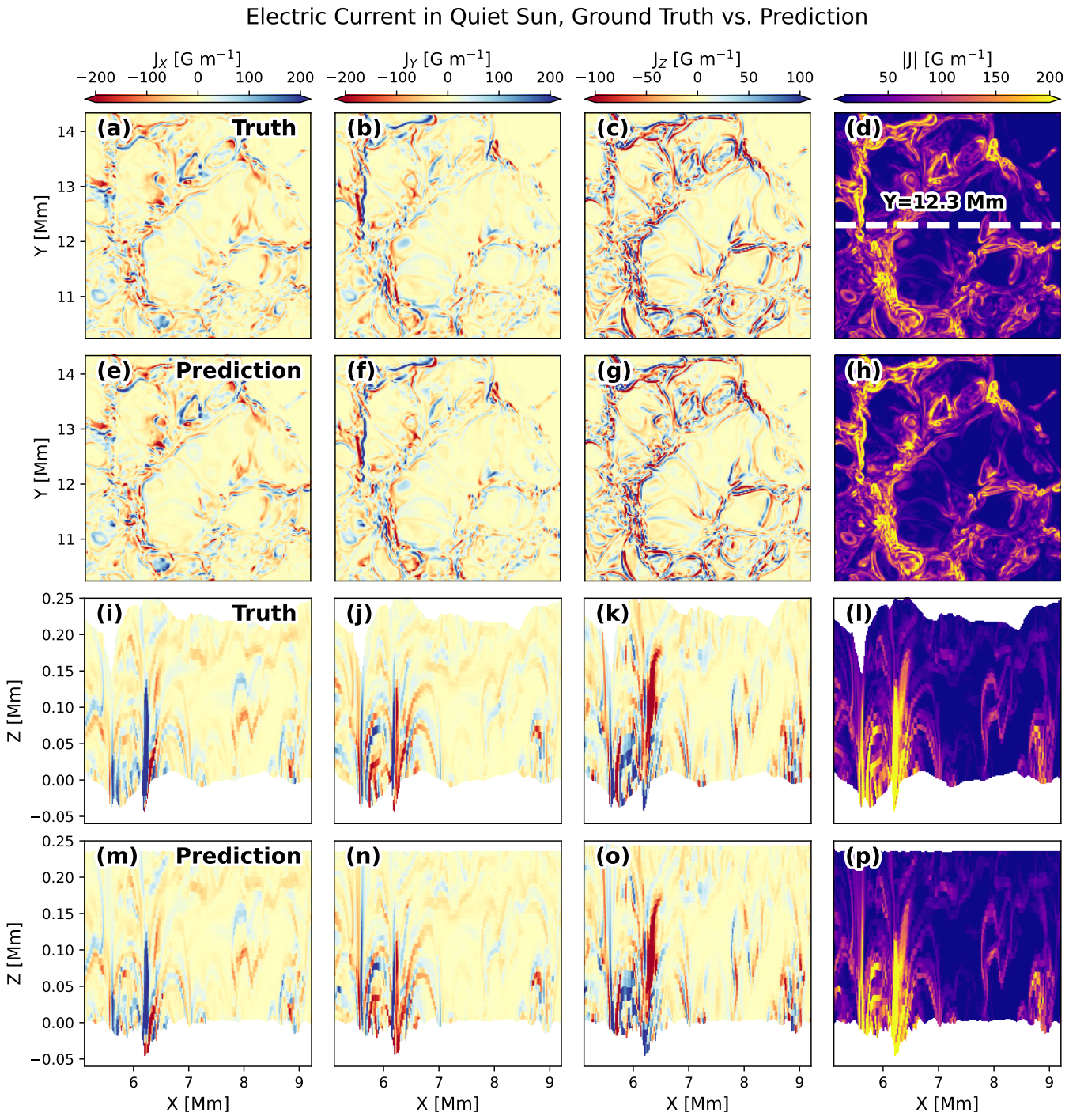


**Figure 12.** Columns from left to right show the x-, y-, z-components, and the absolute value of the electric current in the quiet Sun. Panels (a)–(d) and (e)–(h) display the top view of the electric current on the $\log_{10}\tau = -1$ layer of the ground truth and predictions, respectively. Panels (i)(l) and (m)–(p) present the electric current distribution on the true and predicted vertical cuts at $Y = 12.3$ Mm, indicated by the white dashed line in panel (d).

**Table 1.** HDD Weight Values

| Weight | Value |
|---|---|
| $w_{B_z}$ | $10^8$ |
| $w_{B_t}$ | $10^7$ |
| $w_{parallel}$ | $10^{10}$ |
| $w_{div}$ | $10^8$ |
| $w_{div0}$ [a] | $(10^8-1)\times 0.5\times(\tanh(10\times(\frac{epoch}{20000}-0.5))+1)+1$ |
| $w_{smooth}$ | $10^4$ |
| $w_{mom}$ [b] | $10^{15}$ |

NOTE—

[a] The weight value drop from $10^8$ to 1, the total training take 20,000 total epoches. It is the weight value corresponding to the term $loss_{div0}$, which is used as a rough estimation of the residual flux used for stabilizing the training. Therefore, we signed a large weight at the initial training and dropped to 1.

[b] This weight controls the monotonous property by $loss_{mon}$, which is naturally needed for the prediction; thus, we signed a very large value for it.

gradients if their norm exceeds a threshold proportional to the parameter norm. Then, a value-based clipping with EMA clips gradient values based on an adaptive maximum gradient value computed from the EMA of past gradient magnitudes.

After gradient clipping, the AdamW optimizers (Loshchilov & Hutter 2019) update the model parameters using the computed gradients. The AdamW optimizer is an extension of the Adam optimizer (Kingma & Ba 2015) that includes decoupled weight decay regularization, helping to prevent overfitting by penalizing large weights.

The learning rates for these optimizers are managed by `torch.optim.lr_scheduler.StepLR` schedulers, which adjust the learning rates according to a predefined schedule. The learning rate is initialized at $10^{-3}$ and decays by a factor of 0.5 every 2000 epochs throughout the training process, which spans a total of 30,000 epochs. This step-wise learning rate schedule allows for larger learning rates during the initial phases of training to facilitate rapid learning and exploration of the parameter space. As training progresses, the reduction in the learning rate enables finer adjustments to the model parameters, promoting convergence and helping to avoid overshooting minima in the loss landscape.

By integrating adaptive gradient clipping with dynamic learning rate scheduling and advanced optimization techniques, the training process effectively balances stability and efficiency. This approach ensures that the models not only fit the training data well but also generalize effectively while adhering to the necessary physical constraints of the problem domain.

## 3. TEST

To assess the performance of this method, we applied it to MURaM simulated photospheres, specifically to the quiet Sun, plage region from the SPIn4D dataset (Yang et al. 2024) (transverse spatial resolution $\mathrm{d}x = 16$ km), and a sunspot from Rempel (2012) (spatial resolution $\mathrm{d}x = 32$ km). Figure 3(a)–(c) displays the $B_z$ distribution on the $\log_{10}\tau = -1$ layers for these three cases. For each case, a small sub-region within the FOV is selected (shown in Figure 3(d)–(f)), using optical depths ranging from $\log_{10}\tau = 0$ to $-3.1$ with a sampling of 0.1. These regions are large enough to encompass multiple granules in the quiet Sun and plage regions and include portions of the umbra and penumbra in the sunspot.

The HDD code was applied to all three cases, using ME0 as a baseline for comparison on the same dataset, with parameters listed in Table 2. Most settings are left at default, except for the `bthresh` parameter. Originally intended as a threshold for transverse field strength, `bthresh` activates the nearest-neighbor acute angle method in weak magnetic field regions; however, it was deactivated (set to zero) to enable a fair comparison with the annealing method. For improving accuracy, the cooling rate was set to `tfactr`= 0.999, enabling a gradual annealing process.

Figures 4, 5, and 6 show results for the quiet Sun, plage region, and sunspot, respectively. Each figure presents the disambiguated transverse field and azimuth angle on the $\log_{10}\tau = -1$ surface, comparing ground truth, HDD, and ME0 outputs.

The panels in the first row of Figure 7 provide a statistical analysis with 2D histograms of the angle difference, $\Delta\Phi = \Phi_{pred} - \Phi_{true}$ versus transverse magnetic field magnitude for each case. It is clear that most pixels cluster around zero degrees, indicating a close match between predicted and true angles. From the second to the last rows of Figure 7, we assess the correct recovery rate distribution across transverse magnetic field strengths as the ratio of pixels with an absolute angle difference below 90 degrees ($|\Delta\Phi| < 90°$) to the total number of pixels in each bin. The total number of pixels in each bin for each case is present as the red dash-dot lines. The correct recovery rates from ME0 outputs are also shown for comparison (orange lines). For the quiet Sun and plage regions, recovery rates exceed 90% when $|B_t| > 3$ G and $|B_t| > 7$ G, respectively, while ME0 shows relatively lower rates. In the sunspot case, where the magnetic field is generally stronger, the disambiguation performance is comparable between HDD and ME0.

Figures 8, 9, and 10 show predicted and true geometric heights for each case, including both top views and vertical cuts from selected slices. To eliminate the impact of constant shifts along the $\hat{z}$ direction, both predictions and true values

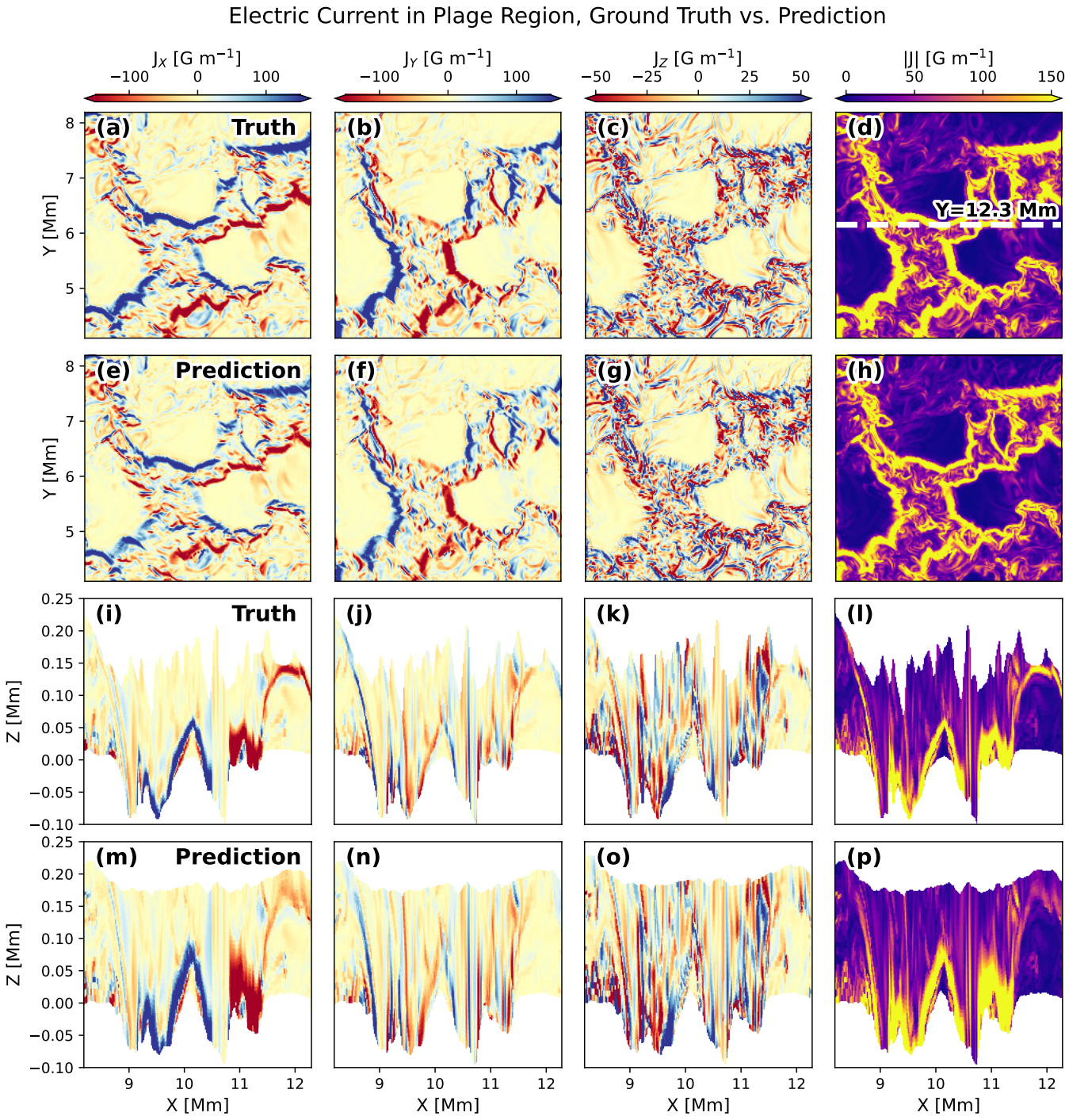


**Figure 13.** The same as Figure 12 but for the plage region results.

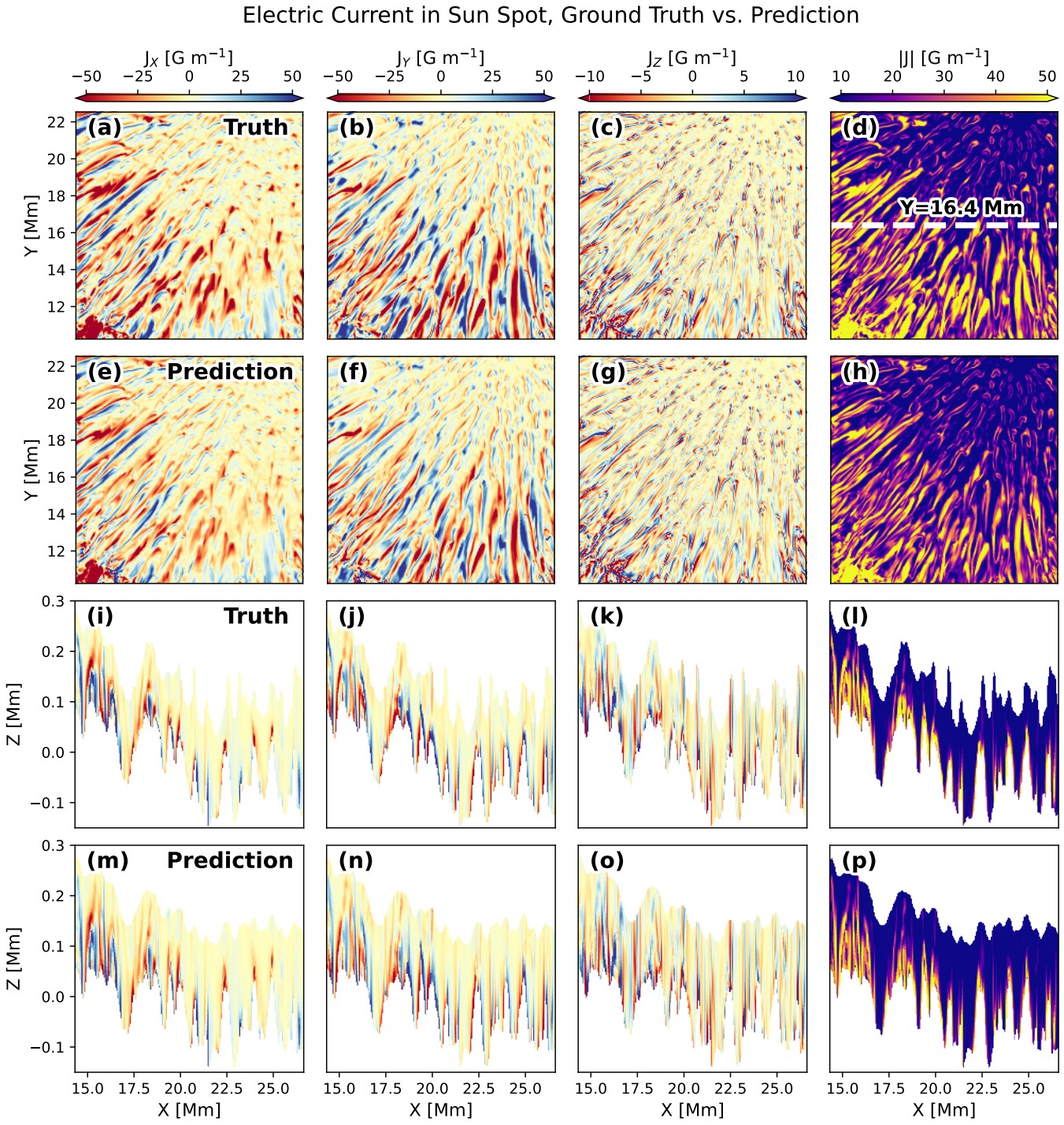


**Figure 14.** The same as Figure 12 but for the sunspot results.

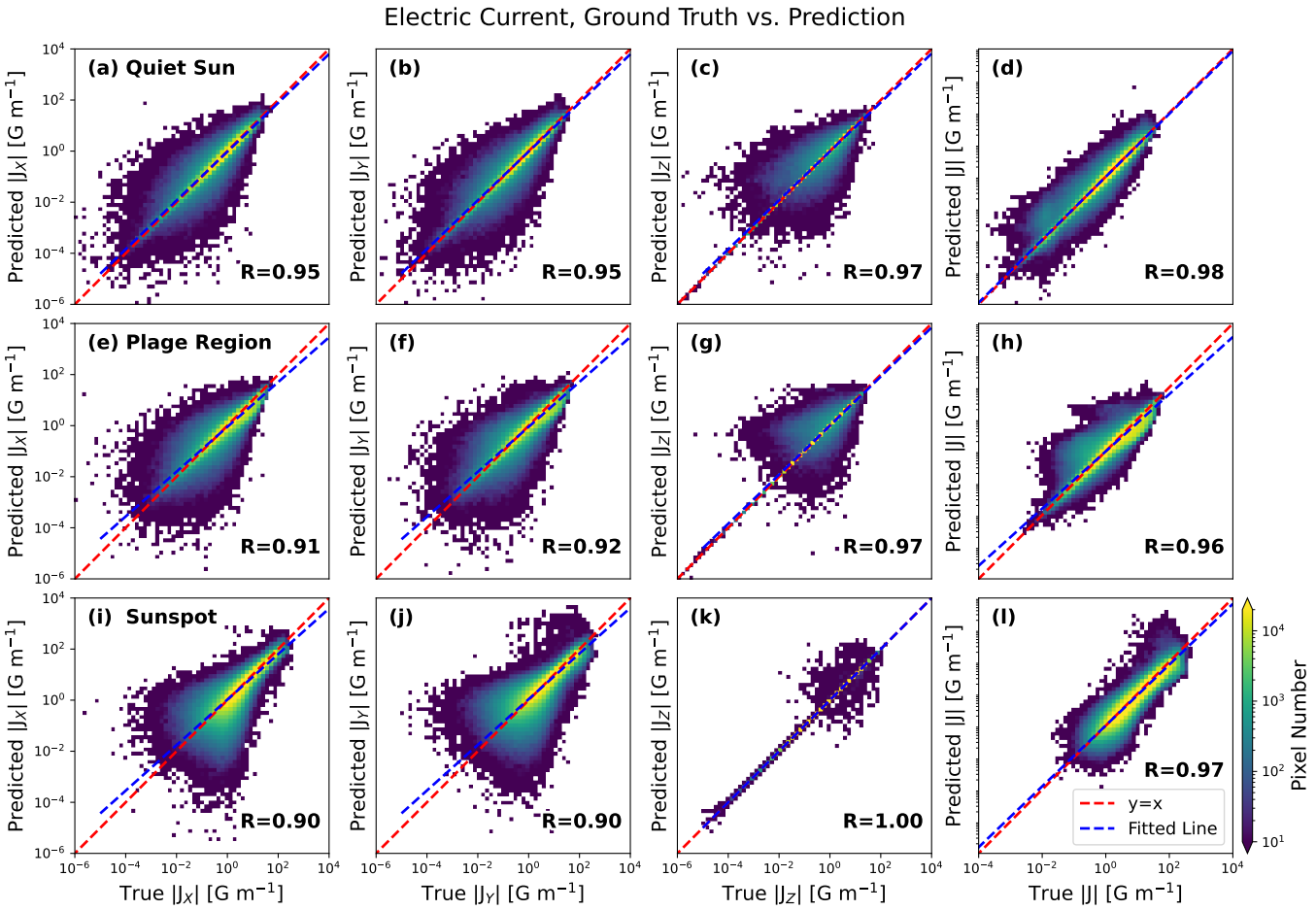


**Figure 15.** 2D histogram comparing ground truth and predicted electric currents. Columns from left to right show the x-, y-, z-components, and absolute current magnitude, while rows from top to bottom represent results for the quiet Sun, plage region, and sunspot, with Pearson correlation coefficients specified for each case. Red and blue dashed lines denote the identity and fitted lines, respectively.

are re-centered, setting the median height of the $\log_{10}\tau = 0$ layer to zero. The height distributions from $\log_{10}\tau$ surfaces of $-0.5$, $-1$, $-1.5$, $-2.0$, and $-2.5$ are represented by black dashed lines in panels (c)–(f) of Figures 8, 9, and 10.

Figure 11 presents 2D histograms comparing predicted and true geometric heights for each case. Pearson correlation coefficients are 0.98, 0.93, and 0.96 for the quiet Sun, plage region, and sunspot, respectively. A $|B_t|$ weighted least-squares linear fits are presented as blue dashed lines.

The vector electric current $J = \nabla \times B$ (neglecting the constant $c/4\pi$) is calculated using the predicted magnetic field as a reference field to disambiguate the azimuth angle and the predicted geometric height. Specifically, the predicted azimuth angle $\Phi_{pred}$ is used to determine whether to flip $\Phi_{obs}$; if the absolute difference exceeds 90 degrees, 180 degrees is added to $\Phi_{obs}$. Figures 12, 13, and 14 present comparisons of the predicted and true vector electric currents for each case. Panels (a)–(h) display distributions on the $\log_{10}\tau = -1$ surface, while panels (i)–(p) show distributions on the vertical slice indicated by the white dashed line in panel (d). Figure 15 provides 2D histograms comparing each vector component and absolute magnitude for each case, with a linear fit performed in log-log space. Pearson correlation coefficients for the $\log_{10}$ absolute values are noted for each case. All correlations are at least 0.9, with 2D histograms showing concentration along the identity line, $y = x$. Similar comparisons of the Lorentz force are shown in Figures 16, 17, and 18. The statistic 2D histogram comparison indicates that the force can be reconstructed as well.

A summary of results across all cases is provided in Table 3.

## 4. DISCUSSION

### 4.1. *Model and Training*

Our proposed method is based on the UNet3D architecture, effectively handling the three-dimensional data struc-

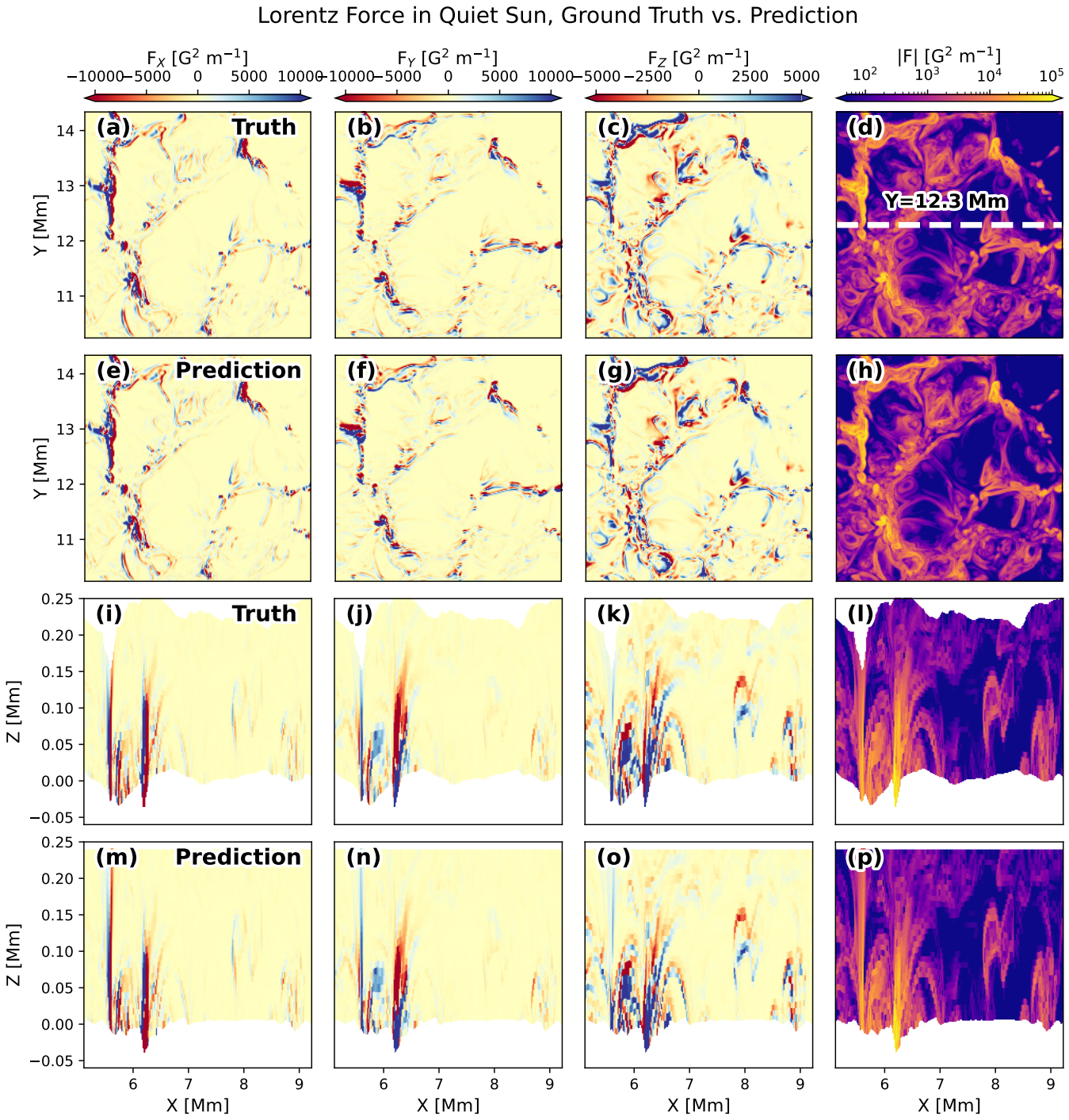


**Figure 16.** The same as Figure 12 but for the Lorentz force distributions.

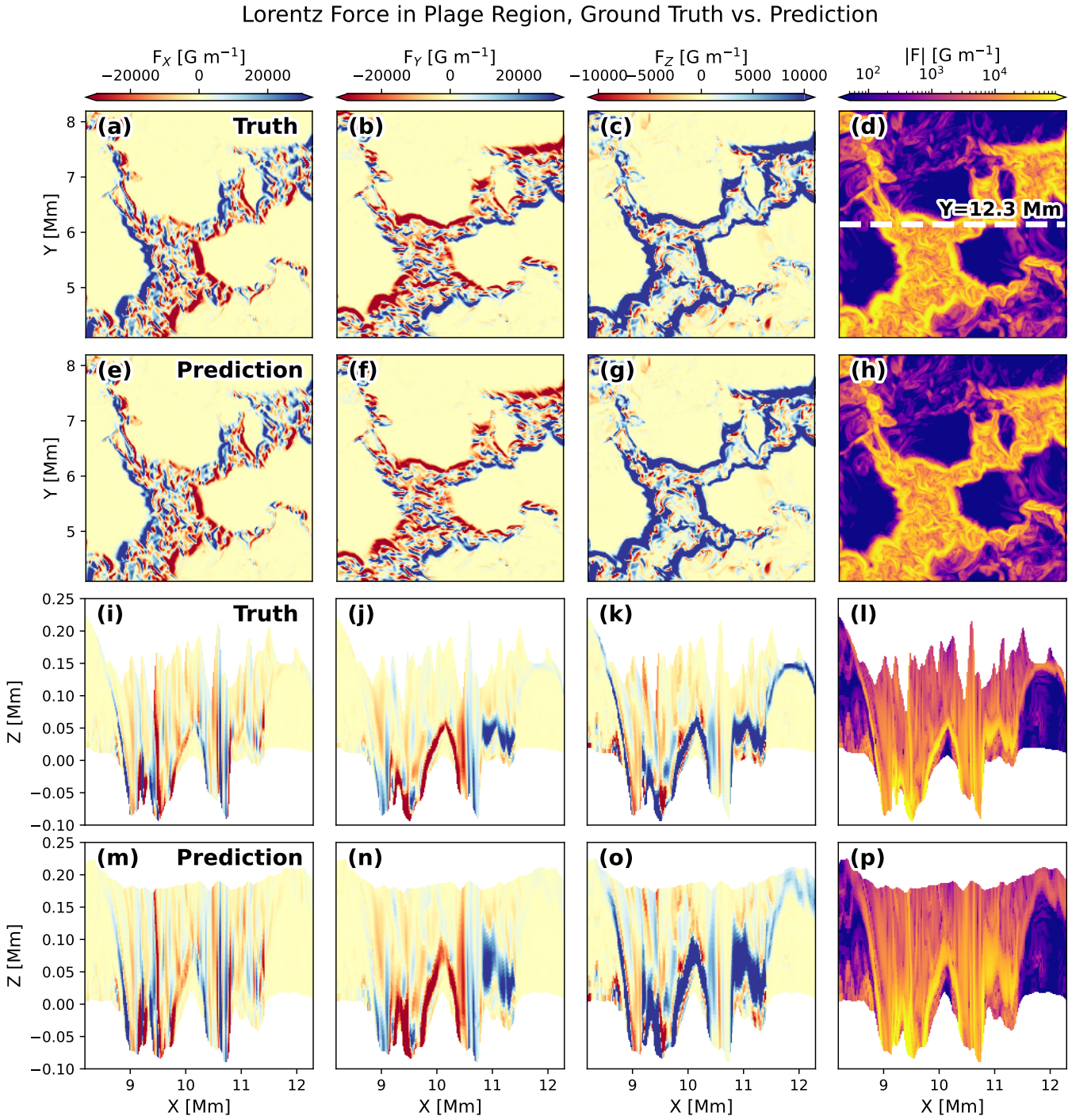


**Figure 17.** The same as Figure 13 but for the Lorentz force distributions.

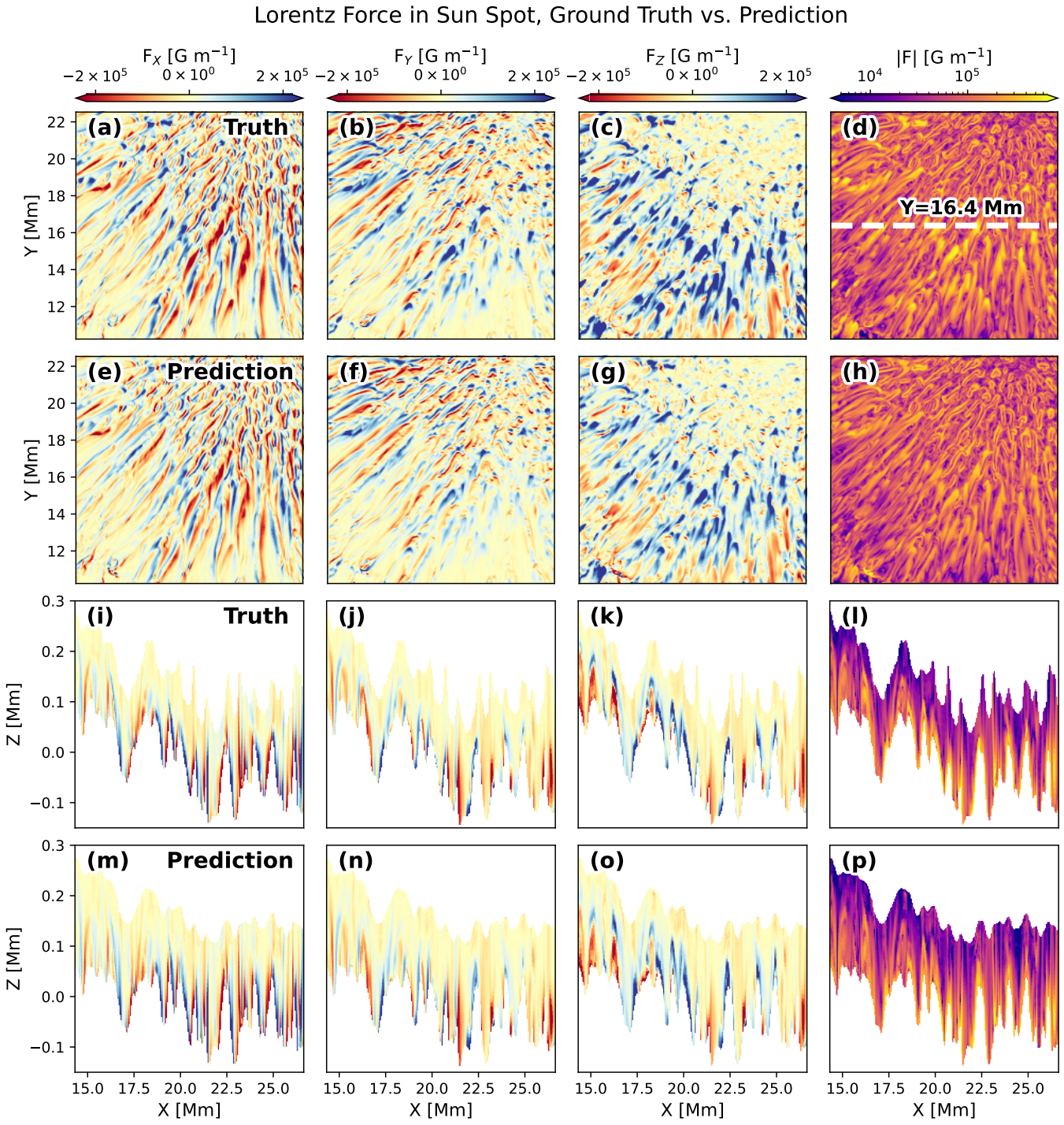


**Figure 18.** The same as Figure 14 but for the Lorentz force distributions.

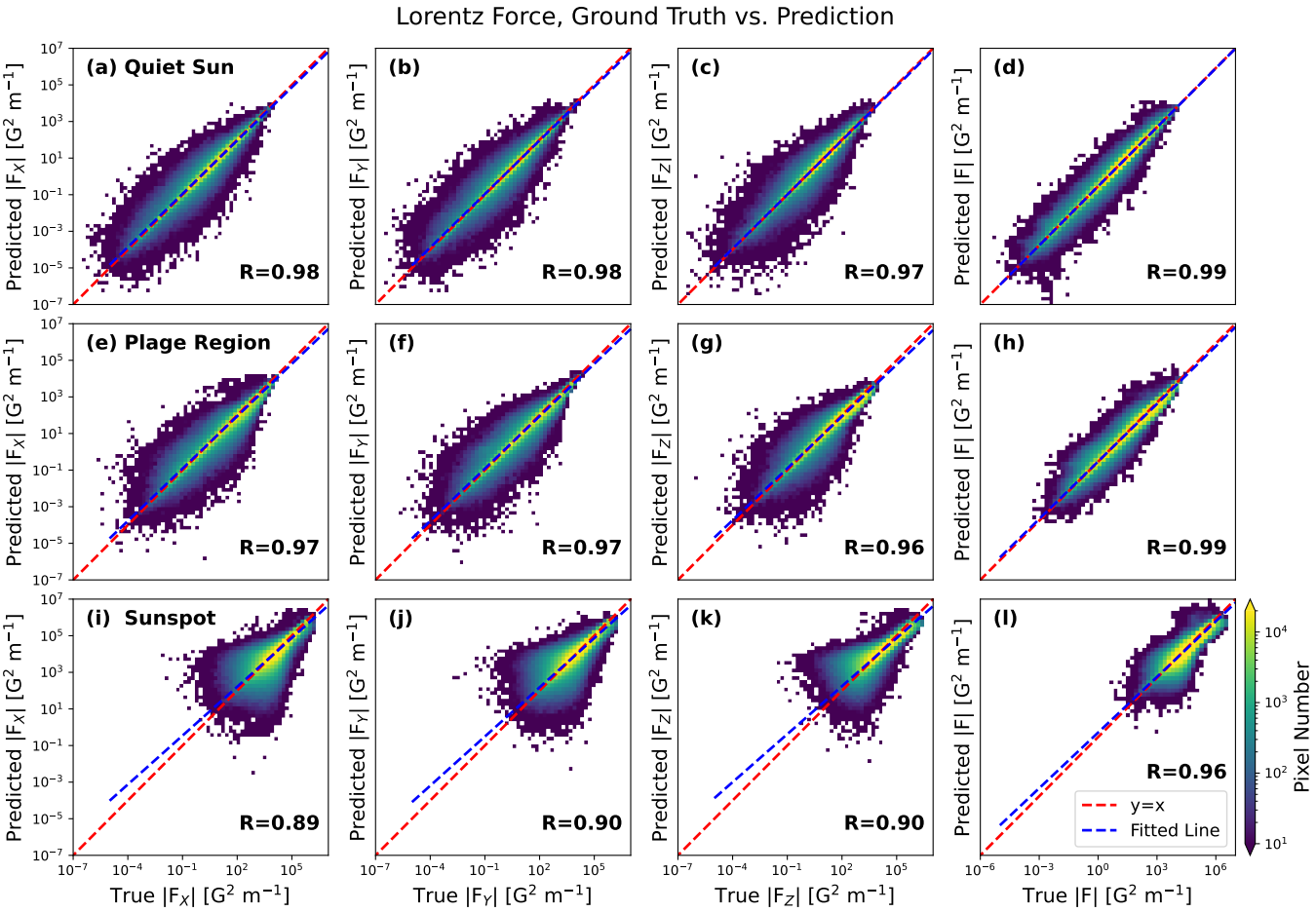


**Figure 19.** The same as Figure 15 but for the Lorentz force comparison.

**Table 2.** ME0 parameters

| Parameter | Value | Parameter | Value |
|---|---|---|---|
| irflag | 0 | nerode | 0 |
| ibflag | 0 | ngrow | 0 |
| iaflag | 0[a] | iaunit | 1 |
| igflag | 1[b] | ipunit | 0 |
| ipflag | 0 | incflag | 0 |
| npad | 200[c] | iseed | 1 |
| nap | 10 | iverb | 1 |
| ntx | 10 | neq | 20 |
| nty | 10 | lambda | 1 |
| athresh | 0 | tfac0 | 2 |
| bthresh | 0 | tfactr | 0.999[d] |

NOTE—

[a] The direction of zero azimuthal angle is along positive $\hat{x}$.

[b] The computation is done on a planar.

[c] The number of pixels added to each side of the field of view.

[d] The cooling rate for the annealing.

**Table 3.** HDD Performance

| | HDD (%)[a] | ME0 (%) | Z (R)[b] | J (R)[c] | F (R)[d] |
|---|---|---|---|---|---|
| Quiet Sun | 93.7 | 69.4 | 0.98 | 0.98 | 0.99 |
| Plage Region | 93.8 | 84.0 | 0.93 | 0.96 | 0.99 |
| Sunspot | 99.9 | 99.3 | 0.96 | 0.97 | 0.96 |

NOTE—

[a] The ambiguity recovery rate for HDD's results is calculated by using the angle of the transverse field predicted by HDD as the reference. A pixel is considered correctly resolved if the predicted angle falls within 90 degrees difference from the ground truth.

[b] Pearson correlation coefficient of the predicted and true geometric heights.

[c] Pearson correlation coefficient of the predicted and true magnitude of vector electric current.

[d] Pearson correlation coefficient of the predicted and true magnitude of Lorentz force.

tures inherent in spectropolarimetric inversions (two spatial dimensions along the FOV and one in optical depth). By employing a learnable model, we leverage the capability of deep learning networks to capture complex spatial patterns and correlations within the data. This enables the model to adapt directly to various solar magnetic field configurations.

One of the significant advantages of our approach is the incorporation of a custom loss function that encodes the divergence-free condition via computation of the residual net flux for each mesh cell. Rather than relying on paired input and target data, the model self-regulates through constraints directly embedding this physical law into the training process, enabling the prediction from the model to inherently satisfy the divergence-free condition, transforming training into a "self-supervised" task. This "self-supervision" enhances the model's ability to generalize to unseen data and reduces dependency on large, labeled datasets, making it more adaptable and robust in handling diverse solar magnetic field configurations.

However, this flexibility introduces the disadvantage of multiple hyperparameters within the custom loss function of this method, adding complexity to the training process. The performance of the UNet3D in this task is sensitive to hyperparameter settings such as weight values listed in Table 1, learning rates, regularization coefficients, batch sizes, and network architecture parameters (e.g., number of layers and channels). Optimizing these hyperparameters requires careful tuning and can be computationally intensive. All the values used for training in this paper are selected after a massive test. In our work, the training process is somewhat complex due to the need to balance various loss functions in Equation 6, like incorporating physical laws and regulation of the magnetic field. The weight values controlling these loss terms are not fully explored and require further investigation to fully understand their impact on the model's performance. Future research could focus on systematically exploring the hyperparameter space using techniques like grid search or Bayesian optimization to achieve optimal results.

It is worth noting that we primarily employ the `ResidualUNet3D` module in our work and have not sufficiently tested it with different layers and channels, we cannot rule out the possibility that other architectures may provide better performance.

Considering its application to real observations, a critical aspect of our method is the need for highly accurate polarization signals and high spatial resolution. As illustrated in Figure 7, the azimuth angle correct recovery rate increases with the transverse magnetic field strength, which relies on the spectropolarimetric inversion of the observed linear polarization signal. Additionally, because we use net flux across each small mesh grid cell, smaller cell scales improve the accuracy of this discrete numerical divergence-free approximation. Consequently, this model is well-suited to take advantage of the capabilities of large ground-based telescopes like DKIST and the future European Solar Telescope (Quintero Noda et al. 2022).

Furthermore, the "self-supervised" nature of this method enables flexible application: it can be used directly on data without pre-training, pre-trained on simulations or pre-exist observations and fine-tuned with new observations, or pre-trained on simulations and applied directly to observational data. By treating the training process as the gradual solving of a PDE for each specific input dataset. This method inherently avoids overfitting a specific dataset, enabling it to perform well even with small datasets, such as the 16 or 36 patches used in our tests. As detailed in Appendix A, the models pre-trained in Section 3 are directly applied to data outside the FOV of the test datasets, demonstrating their adaptability.

### 4.2. *Disambiguation Performance*

Compared to conventional methods like ME0, in which we only work on numerical annealing algorithms without employing nearest neighbor acute angle methods in weak field regions. Our approach demonstrates improved performance in the experiments outlined in Section 3. As shown in Figure 7, the HDD method achieves nearly 100% correct recovery rate of the azimuth angle in strong transverse fields and maintains a high recovery rate even in weaker fields, from quiet Sun to sunspot. For quiet Sun and plage fields around 1 G, and sunspot fields of several hundred Gauss, approximately 80% of pixels correctly predict the azimuth angle orientation ($|\Phi_{pred} - \Phi_{true}| < 90°$). In sunspots, the pixel number distribution differs significantly (red dash-dot lines in Figure 7), with pixels decreasing by about three orders of magnitude from strong to weak field areas. This imbalance in training samples, with fewer weak field examples, results in larger fluctuations in the correct recovery rate compared to quiet Sun and plage regions in the relatively weak field region.

Traditional techniques like ME0 resolve the 180-degree ambiguity by minimizing terms such as $\sum(|J_z|+\nabla\cdot\mathbf{B})$, with $\partial_z B_z$ typically approximated using a potential field based on the inverted LOS field, $B_z$ (Leka et al. 2009a). In contrast, our PIML method integrates the divergence-free condition directly and self-consistently into the learning process. This approach enables more accurate disambiguation across multiple optical depth layers simultaneously without relying on $\partial_z B_z$ from the potential field computation and assuming minimization of the vertical component of the electric current, a constraint that lacks clear physical justification.

In our approach, the divergence-free condition is approximated by calculating the residual net flux across each mesh cell, allowing for easy implementation on an irregular grid with corrugated top and bottom surfaces, shown in Figure 1(a). This feature in the HDD method overcomes the challenges of computing numerical transverse derivatives on a corrugated plane caused by depression, including not only the Wilson depression in sunspots but also those caused by strong magnetic fields in regions like the quiet Sun and plages, resulting in a more physically consistent solution. Notably, we do not use a flipping mask in the network prediction, which will cause the training/solving to blow up. Instead, we leverage (anti-)parallelization by incorporating the square of the cross-product between the predicted and ambiguous transverse magnetic fields, where both parallel and anti-parallel alignments yield a zero value. This term (Equation 3) stabilizes and smooths the training/solving process.

Notably, the training requires tens of thousands of epochs, significantly more than conventional UNet training. In our test cases in Section 3, using two V100 GPUs, each case took approximately 750 minutes, compared to around 250 minutes per case with ME0. However, the fully parallelizable design of the PyTorch-based HDD method allows for significant acceleration when leveraging more GPUs.

Since we test the code with different magnetic environments, including the quiet Sun, plage regions, and sunspots, they present different magnetic field patterns and strength distributions. The tests evidence that this method can work on different magnetic field features and different spatial resolutions and even work with noise input (see Appendix B).

### 4.3. *Geometric Height*

Analysis of the predicted geometric height across optical depth layers reveals that lower layers, such as layers below $\log_{10}\tau = -1.5$, yield more accurate predictions, while higher layers, particularly $\log_{10}\tau = -3.1$, appear smoother in the quiet Sun and plage regions (see Panels (c)–(f) in Figures 8 and 9). Although predictions for sunspot cases are sharper, they still lack the very sharp shape sticking out from the surface shown in the ground truth (Figure 10(c)–(f)). This smoothing effect likely results from the specific form used in the custom loss function (Equation 4), where a fourth power in the numerator and squared magnetic field terms in the denominator prioritize stronger field regions, yielding more accurate solutions.

Overall, the comparisons demonstrate a strong alignment between predictions and ground truth, although the alignment is slightly reduced in the rebinned noisy dataset test (Figure 22). Extensive testing of alternative formulations for regulating residual net flux revealed that the formulation in Equation 4 performs best in our current tests. Future iterations could refine this approach to further improve solutions in the upper atmospheric layers.

Comparing the FIRTEZ code, which integrates spectropolarimetric inversion with disambiguation, iteratively calculates geometric heights using the MHS model (Pastor Yabar et al. 2019; Borrero et al. 2019, 2021; Borrero & Pastor Yabar 2023; Borrero et al. 2024). However, as noted by Vissers et al. (2022), magnetic field structures in the lower solar at-

mosphere derived from non-LTE and weak-field approximations tend to show relatively stronger fields than that from the MHS model extrapolation, particularly for field strengths exceeding 300 G. Moreover, it is known that higher spatial resolution and cadence observations reveal increasingly dynamic structures at smaller scales (Berghmans et al. 2023; Kuridze et al. 2024; Yadav et al. 2024). Considering the pioneering work of Asensio Ramos & Díaz Baso (2019), where networks were trained on Stokes profiles generated from MURaM simulations, applying such methods to real observations (Esteban Pozuelo et al. 2024; Kriginsky & Oliver 2024) would require a large training dataset to encompass the vast parameter space. This challenge is also a key focus of the SPIn4D project, as outlined by Yang et al. (2024). However, a model trained on MURaM inherently produces predictions resembling MURaM simulations, limiting its adaptability to real observations.

Recent advancements in PINN techniques have integrated magnetograms from both the photosphere and chromosphere (Jarolim et al. 2024a). This approach enables estimation of the chromospheric surface height relative to the photosphere through optimal fitting with a non-linear force-free field (NLFFF) model of the 3D magnetic field. The method assumes a flat photospheric plane and zero Lorentz force. While NLFFF models are extensively used to investigate the 3D magnetic field in the solar atmosphere, their validity in regions with weaker magnetic fields remains under debate. Furthermore, higher spatial resolution has revealed more dynamic phenomena, challenging the force-free assumption. Alternatively, the SICON method (Asensio Ramos & Díaz Baso 2019; Esteban Pozuelo et al. 2024; Kriginsky & Oliver 2024) predicts height based on the training dataset, a focus emphasized in the primary goal of SPIn4D project (Yang et al. 2024). In contrast, the HDD approach provides a dynamic-state-independent framework for reconstructing the 3D lower atmosphere. It primarily relies on highly accurate transverse magnetic field data from precise linear polarization observations and remains effective even with very small datasets, offering a significant advantage in practical applications.

In comparison to previous works that estimate geometric heights based on traditional 1D Stokes inversion results (Puschmann et al. 2010; Löptien et al. 2018, 2020), the Wilson depression at each pixel was treated as a free parameter within a merit function minimization framework. These approaches are constrained by high degrees of freedom (DOF) and the limitations of non-convex optimization techniques. In the updated version (Löptien et al. 2018, 2020), they considered the divergence-free condition only and utilized Fourier space, discarding high-frequency signals and consequently losing small-scale structural details. This led to smoother outcomes compared to our method. Using modern ML techniques and advanced optimizers, our approach efficiently searches for local minima in high-DOF optimization, preserving finer structural information.

In addition to the high DOF associated with representing the geometric height at each pixel as a floating-point number, the ambiguity problem introduces two possible orientations per pixel. For a grid of approximately $100 \times 100 \times 30$ pixels, this results in $2^{3\times10^5} \approx 10^{10^5}$ possible combinations. For real observations with grids up to $1000 \times 1000 \times 30$, the choices expand to $2^{3\times10^7} \approx 10^{10^7}$. To handle realistic observations, the input data can be scaled by increasing the input patches, enabling this PIML method to address DOFs exceeding $10^{10^7}$ while accounting for the additional complexity of predicting the geometric height for each pixel.

### 4.4. *Vector Electric Current in 3D Atmospehre*

Our method accurately captures both the morphology (Figures 12, 13, and 14) and magnitude (Figure 15) of electric currents, with predictions closely aligning with ground truth values, the rebinned noisy test presents a similar results (Figure 23). Notably, the accuracy is highest in lower optical depth layers where the magnetic field strength is greater, leading to a more reliable transverse field disambiguation. At higher atmospheric layers, some smoothing is observed, likely due to the loss function's emphasis on strong-field regions as mentioned in Section 4.3. Overall, these results demonstrate the model's capability to reconstruct vector current structures accurately while also indicating areas where dynamic events might happen.

The electric current distributions reveal valuable insights into magnetic structures and dynamics across various solar regions. Measuring electric currents in the solar atmosphere is essential for mapping magnetic fields and understanding their behavior, particularly within sunspots and active regions. Spectropolarimetric inversion techniques reveal complex magnetic structures, with currents varying in strength and orientation, indicative of the twisting and torsion within sunspots. Such variations imply that field-aligned currents are rare, suggesting that sunspots deviate from a force-free state (Socas-Navarro 2005b,a). High-resolution data from instruments like SPINOR, which captures Ca II and Fe I lines, underscore the importance of detailed current density mapping to improve our understanding of solar magnetic processes.

Understanding electric currents in the photosphere and chromosphere is critical to theories of magnetic energy dissipation. Observations show filamentary current structures at chromospheric heights, often extending vertically as sheets near boundary regions like the umbra-penumbra interface (Tan 2007; Anan et al. 2021). This filamentary organization suggests a connection to chromospheric heating, though the underlying mechanisms remain complex. The observed

weak correlation between current density and temperature (Socas-Navarro 2005b,a) highlights the intricate dependencies in energy transfer processes, further emphasizing the need for precise current density measurements. Such kind of sheet-like electric current structures are also presented in our test dataset (shown in Figures 12, 13, 14), which can be reconstructed by this novel method, HDD.

Advanced inversion methods, such as those by Puschmann et al. (2010) and Borrero & Pastor Yabar (2023), often incorporate MHS assumptions, balancing magnetic, pressure, and gravitational forces to estimate current densities in regions where force-free conditions do not apply. However, MHS methods have limitations, particularly at greater heights where pressure forces are weaker, which affects current structure accuracy. Understanding these constraints enables a more accurate interpretation of solar atmospheric data, especially when working in upper layers. It is worth noting that directly comparing the electric current predictions from the FIRTEZ code with ours is not entirely appropriate, as their approach also includes inversion from Stokes profiles, which introduces additional limitations in the weak field region.

Accurate current measurements not only enhance structural understanding but also inform broader theories of energy transport within the solar atmosphere. Electric currents contribute to the formation of magnetic flux tubes, current sheets, and structures related to solar flares and eruptions. Observations of magnetically driven substructures in the chromosphere, such as polarity inversion lines (Vissers et al. 2022), illustrate the fine-scale magnetic complexity that currents produce. The MHS assumption tends to smooth out these substructures compared to direct observations, demonstrating the value of both observational and theoretical approaches for a comprehensive understanding of solar activity.

Moreover, our method facilitates the derivation of a disambiguated vector magnetic field in the real 3D lower solar atmosphere, allowing for direct computation of the vector electric current, essential for understanding events driven by magnetic energy dissipation (da Silva Santos et al. 2022). The results shown on the vertical slices in Figure 12 clearly show the capability to reconstruct the current sheet-like structure in the lower photosphere, however, the existence and properties of those sheets in photosphere are unclear and less explored in the real observations.

### 4.5. *Lorentz Force in 3D Atmospehre*

Using the 3D disambiguated vector magnetic field and electric current, we calculate the Lorentz force as $\vec{F} = \vec{J} \times \vec{B} = (\nabla \times \vec{B}) \times \vec{B}$, omitting the constant $c/4\pi$. Figures 16, 17, and 18 compare the predicted Lorentz force with the ground truth, showing their distribution at $\log_{10} \tau = -1$ and vertical slices through the center of the test datasets. They exhibit a strong morphological agreement. Moreover, the magnitude comparison is shown in Figure 18, suggesting the good alignment across around 6 orders in plage regions and quiet Sun, while the Sunspot presents a range of four orders. The Pearson correlation coefficient of the logarithmic absolute values of each component in plage and quiet Sun demonstrates high accuracy, with a minimum of $0.96$ for $F_Z$ of plage region. Compared with the quiet Sun and plage region, the Sunspot region shows a slightly lower correlation, it remains $0.89$.

Our method provides a direct way to measure the 3D distribution of the Lorentz force quantitatively in the lower solar atmosphere. In many cases, the NLFFF is widely used to model the solar coronal magnetic field by using the photospheric or chromospheric magnetic field as the bottom boundary (Wiegelmann & Sakurai 2021, and references therein). The photospheric magnetic fields do not follow the force-free condition exactly, but the chromospheric magnetic field seems to follow the force-free condition (Metcalf et al. 1995). Unfortunately, chromospheric magnetic field measurements are limited. Many data analyses depend on the force-free assumption, like the twist distribution is usually estimated by the force-free parameter, $\alpha = J_z/B_z$ (Wheatland 2000; Liu et al. 2014) and energy estimation based on MHD virial theorem (Low 1982; Wheatland & Metcalf 2006) that assume the Lorentz force is confined to a thin layer near the photosphere. Those assumptions are not fully investigated in the 3D high spatial-resolved observations. As noted by Socas-Navarro (2005b), electric currents and magnetic fields are generally not aligned, indicating non-force-free conditions, a key insight for modeling dynamic solar processes. The conventional method to check the departure of the force-freeness condition of magnetograms usually comes from the net Lorentz force from a surface integral of the Maxwell stress tensor (Low 1985; Zhang & Zhang 2023). Considering the surface integral over the corrugated optical depth layers, the final results from ours are expected to produce an additional contribution from the strong field region, specifically the edge of the strong field region (see Figures 16, 17, and 18), where the previous measurements are limited. In addition to the distribution, Figure 19 demonstrates the strong alignment of the Lorentz force magnitude. The comparison results for the rebinned noisy dataset, shown in Figure 24, reveal a satisfactory agreement with the prediction as well.

Apart from the Lorentz force linked to the steady evolution of magnetic fields, some magnetic imprints have been observed in response to sudden solar eruptions (Wang et al. 2002; Liu et al. 2012, 2016, 2018; Sun et al. 2017; Xu et al. 2018). These imprints may be attributed to the downward counterpart of the coronal Lorentz force that accelerates the eruption, acting to conserve momentum (Hudson et al. 2008;

Fisher et al. 2012), or a large-amplitude shear Alfvén wave propagating down from the corona (Wheatland et al. 2018). However, the mechanisms driving these changes remain under debate, particularly phenomena like sunspot rotation during flares (Liu et al. 2016) that whether a strong Lorentz force is responsible, e.g., how can a tail wags the dog (Aulanier 2016). The HDD method offers a potential approach to investigating the evolution of such forces, particularly when combined with high-SNR observations.

## 5. SUMMARY

In summary, this innovative method offers a new approach to post-process inversion results from spectropolarimetric observations by leveraging PIML. Its key features are as follows:

1. The method integrates UNet3D with physical laws, utilizing finite numerical techniques in a custom loss function for accurate modeling.

2. It enables simultaneous disambiguation of the vector magnetic field and reconstruction of the lower solar atmosphere's geometry. This requires highly accurate magnetic field inversion across multiple optical depth layers with high spatial resolution.

3. The method allows for the derivation of the 3D vector electric current distribution using Amèpre's law, achieving a high correlation with ground truth values.

4. Training is somewhat time-consuming, while can be accelerated with multiple GPUs, requiring approximately $10^4$ iterations.

Although tested on simulated data, the model's adaptability suggests it could be retrained for real observational data, accounting for potentially different data patterns. Since it is a "self-supervision" property, it can solve the problem specifically from each new dataset, effectively operating as a learnable PDE solver. Additionally, its weight values can be adjusted to optimize performance across diverse datasets. Future enhancements could include incorporating time-series data to strengthen its capabilities further.

This work is supported by NSF/AAG award #2008344. X. Sun is additionally supported by NSF CAREER award #1848250 and the state of Hawai'i. J. Liu acknowledges the support of the DKIST Ambassador program. We thank K. D. Leka and G. Barnes for their valuable input. (To be removed if they agree to coauthor.) We would like to acknowledge the GPU cluster at the Institute for Astronomy, University of Hawai'i at Mānoa, and the high-performance computing support from *Cheyenne* (doi: 10.5065/D6RX99HX) provided by NCAR's Computational and Information Systems Laboratory, sponsored by the NSF.

*Software:* `PyTorch` (Paszke et al. 2019), `Matplotlib` (Hunter 2007), `SciPy` (Virtanen et al. 2020), `Numpy` (Harris et al. 2020), `pytorch-3dunet` (Wolny et al. 2020), and `Haleakala Disambiguation Decoder`.

# APPENDIX

## A. MODEL PERFORMANCE ON UNSEEN DATA

The HDD model can be regarded as a learnable PDE solver capable of learning patterns from data to solve the divergence-free equation. To evaluate its learning capabilities, we applied the model to an untrained dataset. The results are presented in Figure 20. The training data is enclosed within the black dashed boxes, while the margin region represents areas where the equation is not explicitly solved but instead handled directly by the trained network.

The predicted azimuth angle and geometric height are compared with the ground truth. The results demonstrate that the trained data aligns well with the ground truth, while predictions for the untrained data also provide reasonably accurate solutions. This highlights the model's capacity to generalize beyond its training domain.

## B. MODEL PERFORMANCE ON NOISY DATA

To evaluate the performance of the HDD code under realistic observational conditions, we conducted tests using noisy rebinned data. Gaussian noise with a standard deviation of 10 G was added to the quiet Sun and plage region datasets, and 100 G to the sunspot dataset. The original data were then rebinned by $2 \times 2$ to mimic the spatial resolution of DKIST, resulting in spatial resolutions of $\mathrm{d}x = 32$ km for the quiet Sun and plage, and $\mathrm{d}x = 64$ km for the sunspot regions (while DKIST is capable of observing sunspots at much higher resolutions, these values represent a typical resolution range for the dataset used here). To simulate observational data processing, a 3D median filter with a kernel size of $3 \times 3 \times 3$ was applied before running the

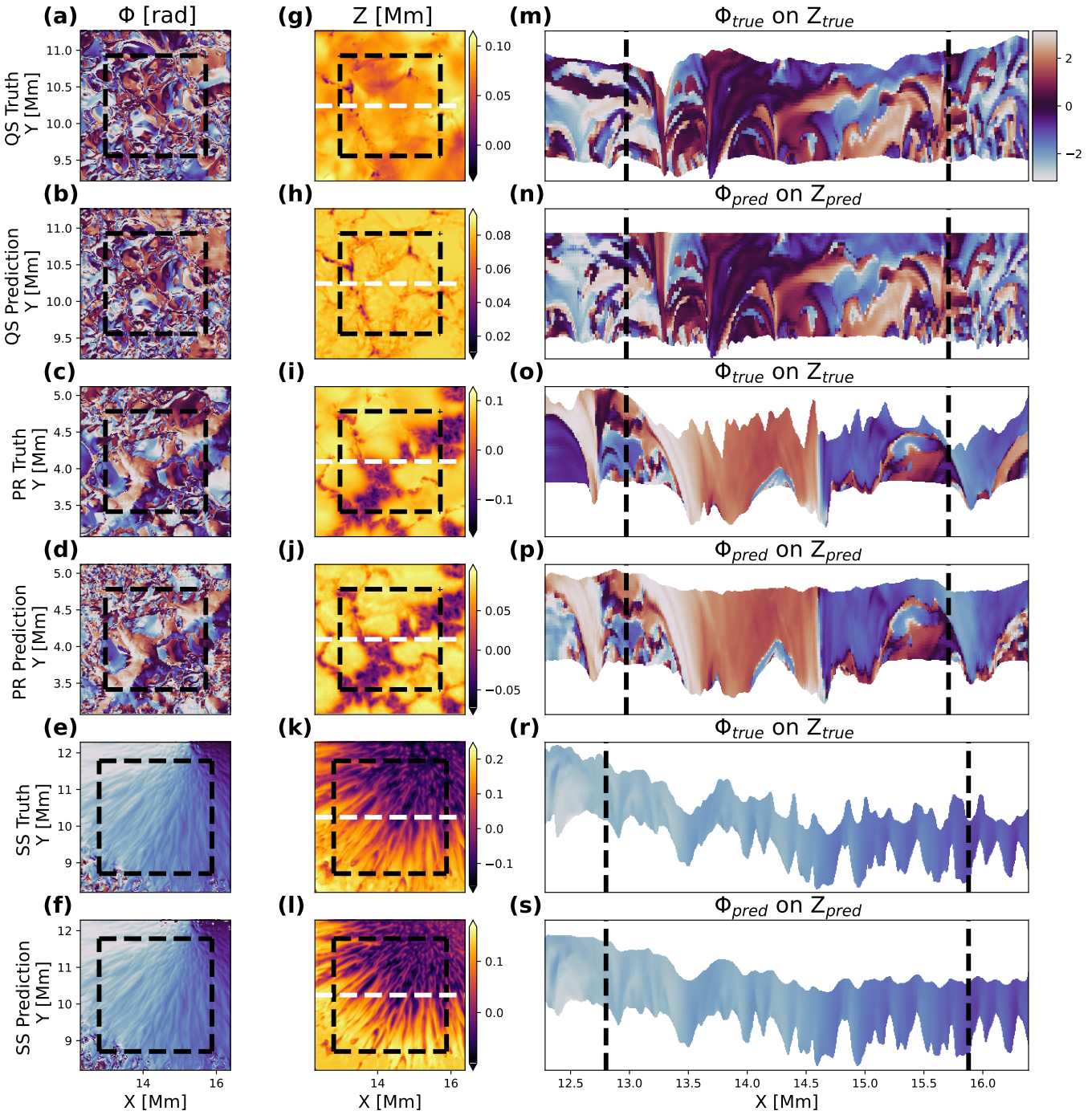


**Figure 20.** Columns from left to right show the predicted azimuth angle on $\log_{10}\tau = -1$ surfaces ((a)–(f)), geometric height on $\log_{10}\tau = -1$ surfaces ((g)–(l)), and angle distribution along vertical cuts ((m)–(s)), respectively. Rows from top to bottom display the ground truth and predictions for the quiet Sun (QS), plage region (PR), and sunspot (SS), respectively. Black dashed lines enclose the regions used for model training, while the white dashed line marks the location of the vertical slice.

HDD code on the dataset. In order to handle the uncertainties of the transverse field, we modify the magnetic field regulation (Equation 2 and Equation 3).

$$loss_{B_t} = \text{mean}\left(\frac{\max\{(B_{x,pred}^2 + B_{y,pred}^2 - B_{x,input}^2 - B_{y,input}^2)^2 - B_{t,err}^4, 0\}}{B_{x,input}^2 + B_{y,pred}^2 + 10^{-8}}\right), \tag{B1}$$

$$loss_{parallel} = \text{mean}\left(\frac{\max\{(B_{x,pred}B_{y,input} - B_{y,pred}B_{x,input})^2 - E_{parallel}, 0\}}{|B_{input}|^2 + 10^{-8}}\right), \tag{B2}$$

where $B_{t,err}$ is the uncertainties of transverse field, i.e., 10 G for the quiet Sun and plages, and 100 G for the sunspot. The error of the parallelization is formulated as $E_{parallel} = \max\{E_{parallel,1}, E_{parallel,1}\}$, where

$$E_{parallel,1} = ((B_{x,input} + B_{t,err})B_{y,input} - (B_{y,input} - B_{t,err})B_{x,input})^2,$$
$$E_{parallel,1} = ((B_{x,input} - B_{t,err})B_{y,input} - (B_{y,input} + B_{t,err})B_{x,input})^2.$$

The recovery rates for each case are illustrated in Figure 21, showing that the azimuth angle orientation is accurately recovered when the transverse field is strong. However, due to the applied noise and median filter, the processed azimuth angle does not perfectly align with the ground truth, particularly in weak field regions. This misalignment results in a more diffuse distribution of the angle difference, $\Delta\Phi = \Phi_{pred} - \Phi_{true}$, compared to Figure 11. Despite a noise level of 10 G, the recovery rate in both the quiet Sun and plages remains close to 80% at 20 G. The quiet Sun exhibits better performance than the ME0 method, while both methods show comparable results in the plages. In the sunspot case, where noise levels reach approximately 100 G, the HDD results indicate a correct recovery rate exceeding 80% for approximately $|B_t| > 300$ G. Overall, the recovery performance under noisy, low spatial resolution conditions is less than the results obtained from high-resolution datasets presented in Section 3.

The comparison between predicted and true geometric heights in noisy cases is shown in Figure 22. While the Pearson correlation coefficients are slightly lower than those from less noisy, high-resolution datasets, they still exhibit a strong correlation with the ground truth. Similar trends are observed for the associated electric current (Figure 23) and Lorentz force (Figure 24), where the correlations, though weaker than in the ideal noise-free scenarios presented in Section 3, remain sufficiently high to demonstrate the reliability of the HDD method and its applicability to real observations.

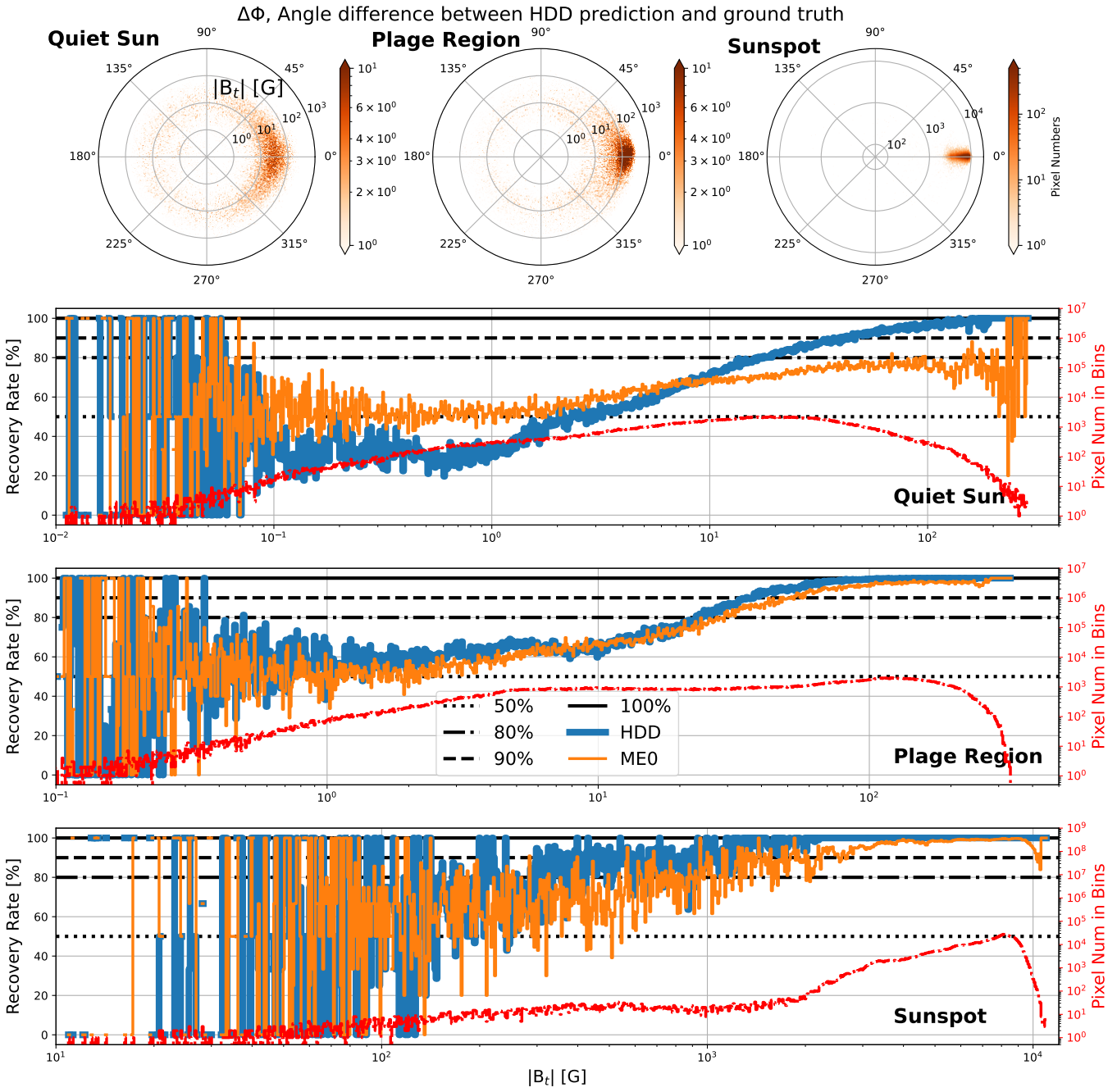


**Figure 21.** The Same as Figure 7 but for the results from the noisy rebinned dataset.

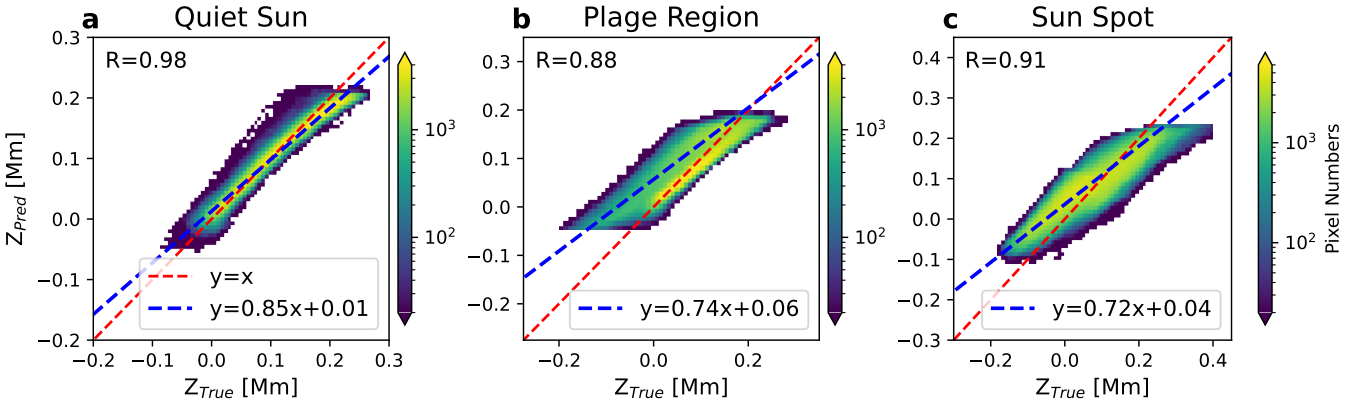


**Figure 22.** The Same as Figure 11 but for the results from the noisy rebinned dataset.

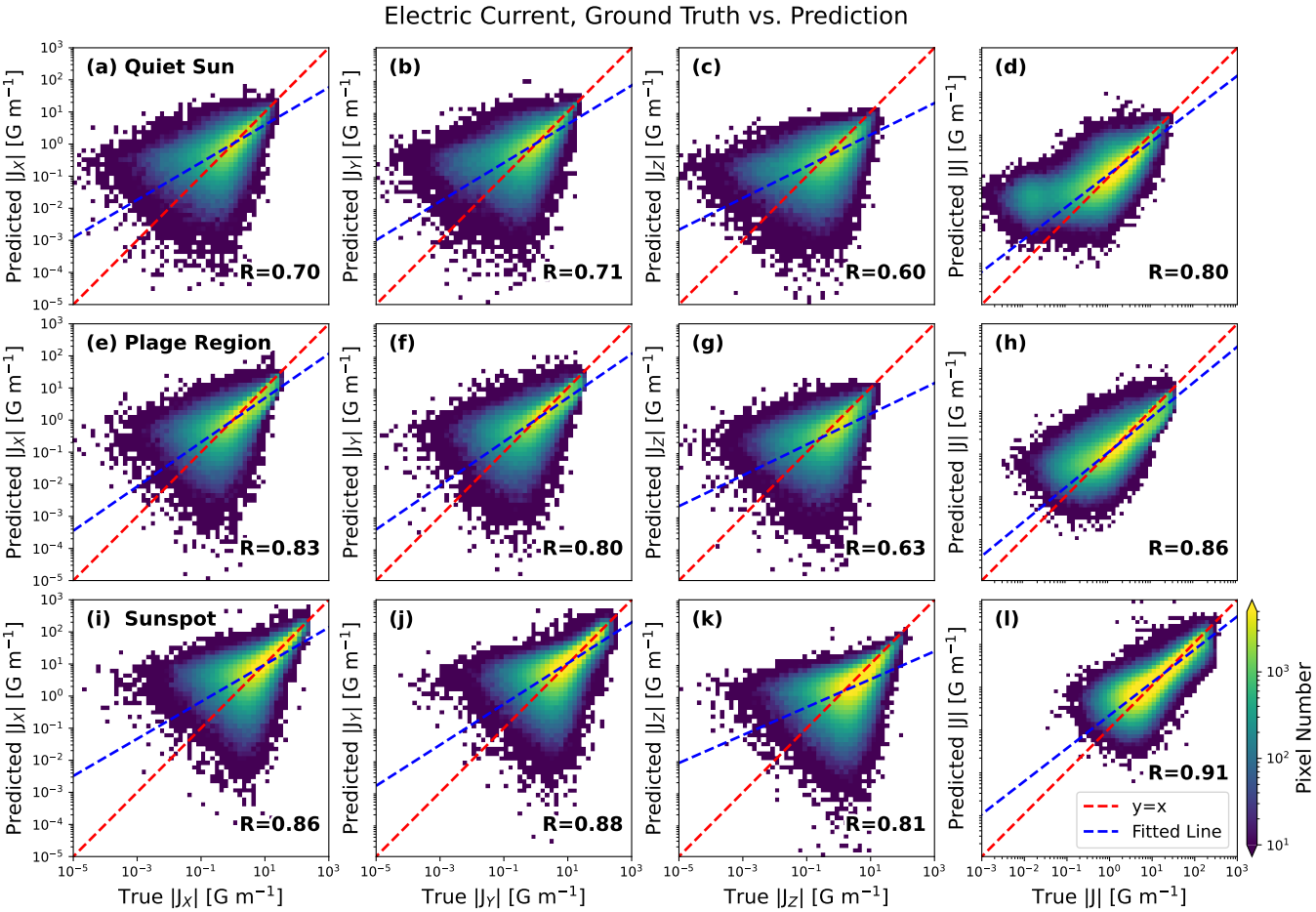


**Figure 23.** The Same as Figure 15 but for the results from the noisy rebinned dataset.

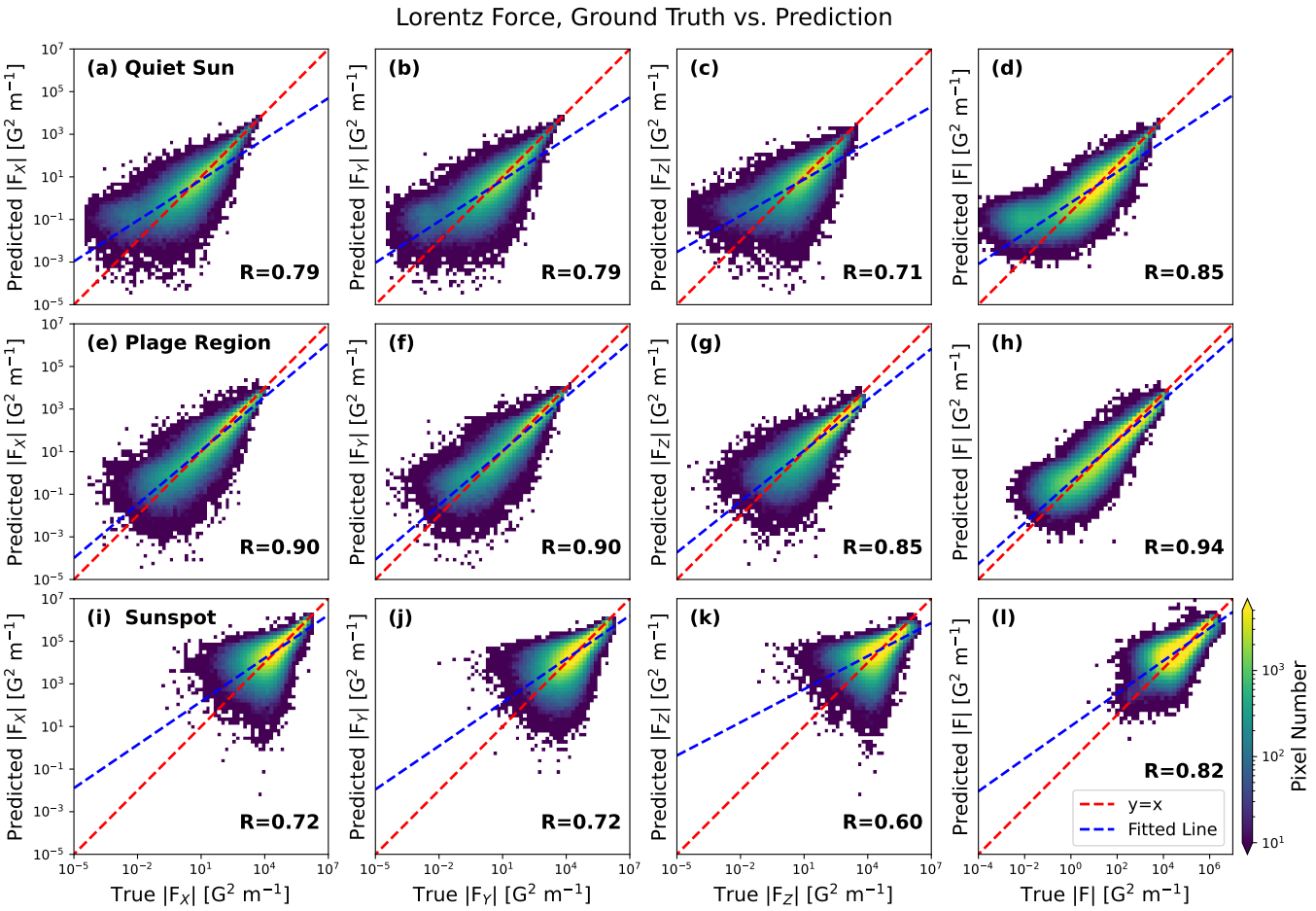


**Figure 24.** The Same as Figure 19 but for the results from the noisy rebinned dataset.

## REFERENCES


Anan, T., Schad, T. A., Kitai, R., et al. 2021, ApJ, 921, 39

Asensio Ramos, A., Cheung, M. C. M., Chifu, I., & Gafeira, R. 2023, Living Reviews in Solar Physics, 20, 4

Asensio Ramos, A. & Díaz Baso, C. J. 2019, A&A, 626, A102

Asensio Ramos, A., Trujillo Bueno, J., & Landi Degl'Innocenti, E. 2008, ApJ, 683, 542

Aulanier, G. 2016, Nature Physics, 12, 998

Barnes, G., Leka, K. D., & Wagner, E. 2018, in Catalyzing Solar Connections, 116

Bellot Rubio, L. & Orozco Suárez, D. 2019, Living Reviews in Solar Physics, 16, 1

Berghmans, D., Antolin, P., Auchère, F., et al. 2023, A&A, 675, A110

Bianda, M., Berdyugina, S., Gisler, D., et al. 2018, A&A, 614, A89

Bobra, M. G. & Couvidat, S. 2015, ApJ, 798, 135

Borrero, J. M. & Pastor Yabar, A. 2023, A&A, 669, A122

Borrero, J. M., Pastor Yabar, A., Rempel, M., & Ruiz Cobo, B. 2019, A&A, 632, A111

Borrero, J. M., Pastor Yabar, A., & Ruiz Cobo, B. 2021, A&A, 647, A190

Borrero, J. M., Pastor Yabar, A., & Ruiz Cobo, B. 2024, A&A, 687, A155

Çiçek, Ö., Abdulkadir, A., Lienkamp, S. S., Brox, T., & Ronneberger, O. 2016, in Medical Image Computing and Computer-Assisted Intervention – MICCAI 2016, ed. S. Ourselin, L. Joskowicz, M. R. Sabuncu, G. Unal, & W. Wells (Cham: Springer International Publishing), 424–432

da Silva Santos, J. M., Danilovic, S., Leenaarts, J., et al. 2022, A&A, 661, A59

de la Cruz Rodríguez, J., Leenaarts, J., Danilovic, S., & Uitenbroek, H. 2019, A&A, 623, A74

de Wijn, A. G., Casini, R., Carlile, A., et al. 2022, SoPh, 297, 22

del Toro Iniesta, J. C. & Ruiz Cobo, B. 2016, Living Reviews in Solar Physics, 13, 4

Dhara, S. K., Capozzi, E., Gisler, D., et al. 2019, A&A, 630, A67

E, W. & Yu, B. 2018, Communications in Mathematics and Statistics, 6, 6

Elmore, D. F., Lites, B. W., Tomczyk, S., et al. 1992, in Society of Photo-Optical Instrumentation Engineers (SPIE) Conference Series, Vol. 1746, Polarization Analysis and Measurement, ed. D. H. Goldstein & R. A. Chipman, 22–33

Esteban Pozuelo, S., Asensio Ramos, A., Díaz Baso, C. J., & Ruiz Cobo, B. 2024, A&A, 689, A255

Fisher, G. H., Bercik, D. J., Welsch, B. T., & Hudson, H. S. 2012, SoPh, 277, 59

Frutiger, C., Solanki, S. K., Fligge, M., & Bruls, J. H. M. J. 2000, A&A, 358, 1109

Georgoulis, M. K. 2005, ApJL, 629, L69

Hao, Z., Liu, S., Zhang, Y., et al. 2022, ArXiv, abs/2211.08064, abs/2211.08064

Harrington, D. M., Sueoka, S. R., Schad, T. A., et al. 2023, SoPh, 298, 10

Harris, C. R., Millman, K. J., van der Walt, S. J., et al. 2020, Nature, 585, 585

Harvey, J. W. 1969, Magnetic Fields Associated with Solar Active-Region Prominences., PhD thesis, National Solar Observatory, Sunspot New Mexico

Hendrycks, D. & Gimpel, K. 2017, Proceedings of International Conference on Learning Representations

Hennigh, O., Narasimhan, S., Nabian, M. A., et al. 2021, in Computational Science – ICCS 2021, ed. M. Paszynski, D. Kranzlmüller, V. V. Krzhizhanovskaya, J. J. Dongarra, & P. M. Sloot (Cham: Springer International Publishing), 447–461

Higgins, R. E. L., Fouhey, D. F., Antiochos, S. K., et al. 2022, ApJS, 259, 24

Higgins, R. E. L., Fouhey, D. F., Zhang, D., et al. 2021, ApJ, 911, 130

Ho, J., Jain, A., & Abbeel, P. 2020, arXiv preprint arxiv:2006.11239

Hoeksema, J. T., Liu, Y., Hayashi, K., et al. 2014, SoPh, 289, 3483

Hudson, H. S., Fisher, G. H., & Welsch, B. T. 2008, in Astronomical Society of the Pacific Conference Series, Vol. 383, Subsurface and Atmospheric Influences on Solar Activity, ed. R. Howe, R. W. Komm, K. S. Balasubramaniam, & G. J. D. Petrie, 221

Hunter, J. D. 2007, Computing in Science & Engineering, 9, 9

Isensee, F., Jaeger, P. F., Kohl, S. A. A., Petersen, J., & Maier-Hein, K. H. 2021, Nature Methods, 18, 203

Isola, P., Zhu, J.-Y., Zhou, T., & Efros, A. A. 2017, in 2017 IEEE Conference on Computer Vision and Pattern Recognition (CVPR), 5967–5976

Jaeggli, S. A., Lin, H., Onaka, P., et al. 2022, SoPh, 297, 137

Jarolim, R., Thalmann, J. K., Veronig, A. M., & Podladchikova, T. 2023, Nature Astronomy, 7, 1171

Jarolim, R., Tremblay, B., Rempel, M., et al. 2024a, ApJL, 963, L21

Jarolim, R., Veronig, A. M., Purkhart, S., Zhang, P., & Rempel, M. 2024b, ApJL, 976, L12

Jiang, C., Wu, S. T., Feng, X., & Hu, Q. 2016, Nature Communications, 7, 11522

Judge, P. G. 2019, MNRAS, 482, 5542

Karniadakis, G. E., Kevrekidis, I. G., Lu, L., et al. 2021, Nature Reviews Physics, 3, 3

Kashinath, K., Mustafa, M., Albert, A., et al. 2021, Philosophical Transactions of the Royal Society of London Series A, 379, 20200093

Kazachenko, M. D., Fisher, G. H., & Welsch, B. T. 2014, ApJ, 795, 17

Kingma, D. & Ba, J. 2015, in International Conference on Learning Representations (ICLR), San Diega, CA, USA

Kriginsky, M. & Oliver, R. 2024, arXiv e-prints, arXiv:2411.05532

Kuridze, D., Uitenbroek, H., Wöger, F., et al. 2024, ApJ, 965, 15

Kusano, K., Iju, T., Bamba, Y., & Inoue, S. 2020, Science, 369, 587

Landi Degl'Innocenti, E. & Bommier, V. 1993, ApJL, 411, L49

Lee, K., Zung, J., Li, P. H., Jain, V., & Seung, H. S. 2017, ArXiv, abs/1706.00120, abs/1706.00120

Leka, K. D., Barnes, G., & Crouch, A. 2009a, in Astronomical Society of the Pacific Conference Series, Vol. 415, The Second Hinode Science Meeting: Beyond Discovery-Toward Understanding, ed. B. Lites, M. Cheung, T. Magara, J. Mariska, & K. Reeves, 365

Leka, K. D., Barnes, G., Crouch, A. D., et al. 2009b, SoPh, 260, 83

Leka, K. D., Barnes, G., Gary, G. A., Crouch, A. D., & Liu, Y. 2012, SoPh, 276, 441

Liu, C., Cao, W., Chae, J., et al. 2018, ApJ, 869, 21

Liu, C., Deng, N., Liu, R., et al. 2012, ApJL, 745, L4

Liu, C., Xu, Y., Cao, W., et al. 2016, Nature Communications, 7, 13104

Liu, Y., Hoeksema, J. T., Bobra, M., et al. 2014, ApJ, 785, 13

Liu, Y., Hoeksema, J. T., Sun, X., & Hayashi, K. 2017, SoPh, 292, 29

Liu, Y. & Schuck, P. W. 2012, ApJ, 761, 105

Löptien, B., Lagg, A., van Noort, M., & Solanki, S. K. 2018, A&A, 619, A42

Löptien, B., Lagg, A., van Noort, M., & Solanki, S. K. 2020, A&A, 635, A202

Loshchilov, I. & Hutter, F. 2019, in International Conference on Learning Representations

Low, B. C. 1982, SoPh, 77, 43

Low, B. C. 1985, in Measurements of Solar Vector Magnetic Fields, ed. M. J. Hagyard, 49–65

Lu, L., Meng, X., Mao, Z., & Karniadakis, G. E. 2021, SIAM Review, 63, 63

Malherbe, J. M., Moity, J., Arnaud, J., & Roudier, T. 2007, A&A, 462, 753

Mao, Z., Jagtap, A. D., & Karniadakis, G. E. 2020, Computer Methods in Applied Mechanics and Engineering, 360, 112789

Martinez Pillet, V. & Vazquez, M. 1993, A&A, 270, 494

Mathew, S. K., Solanki, S. K., Lagg, A., et al. 2004, A&A, 422, 693

Metcalf, T. R. 1994, SoPh, 155, 235

Metcalf, T. R., Jiao, L., McClymont, A. N., Canfield, R. C., & Uitenbroek, H. 1995, ApJ, 439, 474

Metcalf, T. R., Leka, K. D., Barnes, G., et al. 2006, SoPh, 237, 267

Milić, I. & van Noort, M. 2018, A&A, 617, A24

Moon, Y. J., Wang, H., Spirock, T. J., Goode, P. R., & Park, Y. D. 2003, SoPh, 217, 79

Müller, D., St. Cyr, O. C., Zouganelis, I., et al. 2020, A&A, 642, A1

Pastor Yabar, A., Borrero, J. M., & Ruiz Cobo, B. 2019, A&A, 629, A24

Paszke, A., Gross, S., Massa, F., et al. 2019, ArXiv, abs/1912.01703, abs/1912.01703

Pesnell, W. D., Thompson, B. J., & Chamberlin, P. C. 2012, SoPh, 275, 3

Puschmann, K. G., Ruiz Cobo, B., & Martínez Pillet, V. 2010, ApJ, 720, 1417

Quintero Noda, C., Schlichenmaier, R., Bellot Rubio, L. R., et al. 2022, A&A, 666, A21

Raissi, M. 2018, Journal of Machine Learning Research, 19, 19

Raissi, M., Perdikaris, P., & Karniadakis, G. E. 2019, Journal of Computational Physics, 378, 686

Rempel, M. 2012, ApJ, 750, 62

Rempel, M., Schüssler, M., & Knölker, M. 2009, ApJ, 691, 640

Riethmüller, T. L., Solanki, S. K., Barthol, P., et al. 2017, ApJS, 229, 16

Rimmele, T. R., Warner, M., Keil, S. L., et al. 2020, SoPh, 295, 172

Romero Avila, A., Inhester, B., Hirzberger, J., & Solanki, S. K. 2024, SoPh, 299, 41

Ronneberger, O., Fischer, P., & Brox, T. 2015, in Medical Image Computing and Computer-Assisted Intervention – MICCAI 2015, ed. N. Navab, J. Hornegger, W. M. Wells, & A. F. Frangi (Cham: Springer International Publishing), 234–241

Ruiz Cobo, B. & del Toro Iniesta, J. C. 1992, ApJ, 398, 375

Ruiz Cobo, B., Quintero Noda, C., Gafeira, R., et al. 2022, A&A, 660, A37

Rumelhart, D. E., Hinton, G. E., & Williams, R. J. 1986, Nature, 323, 533

Scherrer, P. H., Schou, J., Bush, R. I., et al. 2012, SoPh, 275, 207

Semel, M. & Skumanich, A. 1998, A&A, 331, 383

Sirignano, J. & Spiliopoulos, K. 2018, Journal of Computational Physics, 375, 375

Socas-Navarro, H. 2005a, ApJL, 633, L57

Socas-Navarro, H. 2005b, ApJL, 631, L167

Socas-Navarro, H., de la Cruz Rodríguez, J., Asensio Ramos, A., Trujillo Bueno, J., & Ruiz Cobo, B. 2015, A&A, 577, A7

Solanki, S. K., del Toro Iniesta, J. C., Woch, J., et al. 2020, A&A, 642, A11

Sun, X., Hoeksema, J. T., Liu, Y., Kazachenko, M., & Chen, R. 2017, ApJ, 839, 67

Tan, B. 2007, Advances in Space Research, 39, 1826

Tsuneta, S., Ichimoto, K., Katsukawa, Y., et al. 2008, SoPh, 249, 167

Valori, G., Calchetti, D., Moreno Vacas, A., et al. 2023, A&A, 677, A25

Valori, G., Löschl, P., Stansby, D., et al. 2022, SoPh, 297, 12
van Noort, M. 2012, A&A, 548, A5
Virtanen, P., Gommers, R., Oliphant, T. E., et al. 2020, Nature Methods, 17, 261
Vissers, G. J. M., Danilovic, S., Zhu, X., et al. 2022, A&A, 662, A88
Vögler, A., Shelyag, S., Schüssler, M., et al. 2005, A&A, 429, 335
Wang, H. 1997, SoPh, 174, 265
Wang, H., Spirock, T. J., Qiu, J., et al. 2002, ApJ, 576, 497
Wang, H., Yan, Y., & Sakurai, T. 2001, SoPh, 201, 323
Wheatland, M. S. 2000, ApJ, 532, 616
Wheatland, M. S., Melrose, D. B., & Mastrano, A. 2018, ApJ, 864, 159
Wheatland, M. S. & Metcalf, T. R. 2006, ApJ, 636, 1151
Wiegelmann, T. & Sakurai, T. 2021, Living Reviews in Solar Physics, 18, 1
Wilson, A. & Maskelyne, N. 1774, Philosophical Transactions of the Royal Society of London Series I, 64, 1
Wolny, A., Cerrone, L., Vijayan, A., et al. 2020, eLife, 9, 9
Wu, Y., Sicard, B., & Gadsden, S. A. 2024, Expert Systems with Applications, 255, 255
Xu, Y., Cao, W., Ahn, K., et al. 2018, Nature Communications, 9, 46
Yadav, R., Kazachenko, M. D., Afanasyev, A. N., Cauzzi, G., & Reardon, K. 2024, ApJL, 973, L10
Yang, K. E., Tarr, L. A., Rempel, M., et al. 2024, ApJ, 976, 204
Zeiler, M. D. & Fergus, R. 2014, in Computer Vision – ECCV 2014, ed. D. Fleet, T. Pajdla, B. Schiele, & T. Tuytelaars (Cham: Springer International Publishing), 818–833
Zeuner, F., Belluzzi, L., Guerreiro, N., Ramelli, R., & Bianda, M. 2022, A&A, 662, A46
Zeuner, F., del Pino Alemán, T., Trujillo Bueno, J., & Solanki, S. K. 2024, ApJ, 964, 10
Zeuner, F., Feller, A., Iglesias, F. A., & Solanki, S. K. 2018, A&A, 619, A179
Zeuner, F., Manso Sainz, R., Feller, A., et al. 2020, ApJL, 893, L44
Zhang, M. & Zhang, H. 2023, ApJL, 956, L17